2007

Star formation in NGC 5194 (M51a). II. The spatially resolved star formation law

RC Kennicutt

D Calzetti

F Walter

G Helou

DJ Hollenbach

See next page for additional authors

Star Formation in NGC 5194 (M51a). II. The Spatially-Resolved Star Formation Law

Robert C. Kennicutt, Jr.[1,2,3], Daniela Calzetti[3,4,5], Fabian Walter[6], George Helou[7], David J. Hollenbach[8], Lee Armus[9], George Bendo[10], Daniel A. Dale[3,11], Bruce T. Draine[12], Charles W. Engelbracht[2,3], Karl D. Gordon[2,3], Moire K.M. Prescott[2], Michael W. Regan[5], Michele D. Thornley[13], Caroline Bot[9], Elias Brinks[14], Erwin de Blok[15], Dulia de Mello[16,17], Martin Meyer[5], John Moustakas[18], Eric J. Murphy[19], Kartik Sheth[9], and J.D.T. Smith[2,3]

ABSTRACT

[1]Institute of Astronomy, University of Cambridge, Madingley Road, Cambridge CB3 0HA, UK

[2]Steward Observatory, University of Arizona, Tucson, AZ 85721

[3]Visiting Astronomer, Kitt Peak National Observatory, National Optical Astronomy Observatory, which is operated by the Association of Universities for Research in Astronomy, Inc. (AURA) under cooperative agreement with the National Science Foundation.

[4]Department of Astronomy, University of Massachusetts, 710 N. Pleasant Street, Amherst, MA 01003

[5]Space Telescope Science Institute, 3700 San Martin Drive, Baltimore, MD 21218

[6]Max-Planck-Institute für Astronomie, Königstuhl 17, Heidelberg, D-69117, Germany

[7]Caltech, MS 314-6, Pasadena, CA 91101

[8]NASA Ames Research Center, MS 245-3, Moffett Field, CA 94035-1000

[9]Spitzer Science Center, Caltech, MS 220-6, Pasadena, CA 91101

[10]Astrophysics Group, Imperial College, Blackett Laboratory, Prince Consort Road, London SW7 2AZ, UK

[11]Department of Physics & Astronomy, University of Wyoming, Laramie, WY 82071

[12]Department of Astrophysical Sciences, Princeton University, Princeton, NJ 08544-1001

[13]Department of Physics and Astronomy, Bucknell University, Lewisburg, PA 17837

[14]School of Physics, Astronomy, and Mathematics, University of Hertfordshire, College Lane, Herts AL10 9AB, United Kingdom

[15]Research School of Astronomy and Astrophysics, Mount Stromlo Observatory, Cotter Road, Weston Creek ACT 2611, Australia

[16]Laboratory for Observational Cosmology, Code 665, Goddard Space Flight Center, Greenbelt, MD 20771

[17]Department of Physics, Catholic University of America, Washington, DC 20064

[18]Physics Department, New York University, 4 Washington Place, New York, NY 10003

[19]Department of Astronomy, Yale University, P.O. Box 208101, New Haven, CT 06520-8101

We have studied the relationship between the star formation rate (SFR) surface density and gas surface density in the spiral galaxy M51a (NGC 5194), using multi-wavelength data obtained as part of the Spitzer Infrared Nearby Galaxies Survey (SINGS). We introduce a new SFR index based on a linear combination of Hα emission-line and 24 μm continuum luminosities, that provides reliable extinction-corrected ionizing fluxes and SFR densities over a wide range of dust attenuations. The combination of these extinction-corrected SFR densities with aperture synthesis HI and CO maps has allowed us to probe the form of the spatially-resolved star formation law on scales of 0.5 to 2 kpc. We find that the resolved SFR vs gas surface density relation is well represented by a Schmidt power law, which is similar in form and dispersion to the disk-averaged Schmidt law. We observe a comparably strong correlation of the SFR surface density with the molecular gas surface density, but no significant correlation with the surface density of atomic gas. The best-fitting slope of the Schmidt law varies from N = 1.37 to 1.56, with zeropoint and slope that change systematically with the spatial sampling scale. We tentatively attribute these variations to the effects of areal sampling and averaging of a nonlinear intrinsic star formation law. Our data can also be fitted by an alternative parametrization of the SFR surface density in terms of the ratio of gas surface density to local dynamical time, but with a considerable dispersion.

Subject headings: galaxies: individual (M51a, NGC 5194) – galaxies: ISM — galaxies: evolution — HII regions – infrared: galaxies — stars: formation

1. Introduction

One of the crucial missing links in our knowledge of star formation and galaxy evolution is an understanding of the interplay between the star formation rate (SFR) in galaxies and the underlying properties of the interstellar medium (ISM). Despite the physical complexity of this relationship, observations of galaxies on global scales reveal a surprisingly tight correlation between the average SFR per unit area and the mean surface density of cold gas, extending over several orders of magnitude in gas surface density (e.g., Kennicutt 1998a, b, and references therein). The most widely used parametrization is the power-law relation introduced by Schmidt (1959, 1963). In this paper we study the surface density form of this relation:

$$\Sigma_{SFR} = A \; {\Sigma_g}^N \tag{1}$$

where Σ_{SFR} and Σ_g refer to the star formation and total (molecular and atomic) hydrogen surface densities, respectively. When measured in units of $M_\odot$ yr^{-1} kpc^{-2} for Σ_{SFR} and $M_\odot$ pc^{-2} for Σ_g the disk-averaged data compiled by Kennicutt (1998b) are best fitted by a power law with slope $N = 1.4 \pm 0.15$ and zeropoint $A = 2.5 \pm 0.7 \times 10^{-4}$. This parametrization has proven to be very useful as an input scaling law for analytical and numerical models of galaxy evolution (e.g., Kay et al. 2002). Throughout this paper we shall deal exclusively with measurements of the surface densities of star formation and gas, even if for the sake of concise text we do not refer explicitly to "surface" density in every instance.

Despite its widespread application, this global law offers little insight into the underlying physical nature of star formation regulation. A surface density power law with $N \sim 1.5$ is consistent with what one would expect if the SFR is mainly driven by large-scale gravitational instabilities in the disk (e.g., Elmegreen 2002). However the disk-averaged star formation rates of galaxies are nearly as well fitted by prescriptions in which the SFR surface density scales with the ratio of gas surface density to local dynamical time (e.g., Silk 1997, Kennicutt 1998b):

$$\Sigma_{SFR} = A' \, \Sigma_g \, \Omega_g \tag{2}$$

where Ω_g is the average angular frequency of the rotating gas disk. Such a relation could be reproduced in a picture in which the SFR per unit gas mass in clouds is constant, and the frequency of cloud formation events scales inversely with the local orbit time, for example the frequency of spiral density wave passages. These scenarios are only cited as illustrative examples; the fact that such different pictures can account for the global SFRs underscores the inability of these data alone to discriminate between different physical origins for the star formation law.

A complementary and in some ways more fundamental approach is to use spatially-resolved measurements of the SFR and gas surface densities to examine the correlations between the observables on a point-by-point basis within galaxies. This allows us to quantify the form of the star formation law across the large ranges in local physical conditions that are found in galaxies. Numerous such studies of the local Schmidt law have been carried out over the last 40 years (see Kennicutt 1997 for a review). Due to the limited spatial resolution of the HI and CO data at the time, most studies were confined to the nearest galaxies, and correlated the SFR with either the atomic or molecular gas surface densities, but rarely both. The SFRs themselves were generally measured using blue star counts, HII region counts, or Hα emission, usually without corrections for extinction. Consequently it is not entirely surprising that the results of these studies have been inconsistent, with the derived power-law slopes (eq. [1]) ranging over $N = 1 - 3$ and beyond (Kennicutt 1997). More recently a number of workers have used radial profiles of gas and SFR surface densities to constrain the form of the Schmidt law on intermediate (typically few kpc) scales (e.g., Martin & Kennicutt 2001, Boissier et al. 2003, Schuster et al. 2007), and again the resulting power law slopes are sensitive to the gas, SFR tracers, and the prescriptions used to correct for extinction and convert the observed CO line intensities into molecular gas surface densities.

The main limiting factors for this work have been the lack of high spatial resolution HI and CO observations of galaxies and of multi-wavelength observations of the star-forming regions, which are necessary to derive accurate extinction-corrected SFR distributions. The situation has improved in recent years with the completion of several aperture synthesis CO mapping surveys of galaxies, most notably the Berkeley Illinois Maryland Association Survey of Nearby Galaxies (BIMA SONG; Helfer et al. 2003). These provide CO maps with synthesized beam sizes of several arcseconds, making it possible to probe the form of the star formation law on sub-kiloparsec scales (e.g., Wong & Blitz 2002). However, dust extinction poses a serious obstacle to these studies. At the high gas column densities probed by SONG, the corresponding dust column densities are large, producing attenuations of up 5 mag (or more) in Hα and the ultraviolet. This is large enough to cause SFRs based on Hα or ultraviolet measurements to be severely underestimated. On the other hand, much of the star formation in disks occurs in regions with low to moderate extinction (<1 mag at Hα), and there estimates of SFRs based solely on the dust emission will also be underestimated. Moreover, since the extinction tends to correlate with the gas surface density itself, dust will bias the slope of the derived star formation law if left uncorrected. Wong & Blitz (2002) used the gas surface density itself to estimate the magnitude of the Hα extinction correction, but as they pointed out this introduces a circularity into the determination of the star formation law, and it would be preferable to measure the attenuation corrections independently of the gas density.

The advent of high-resolution infrared mapping of nearby galaxies with the Spitzer Space Telescope now allows us to undertake a much more rigorous study of the spatially-resolved Schmidt law. The combination of far-infrared, Hα, and Paα maps of galaxies allows us to derive extinction-corrected SFR distributions independently from the CO and HI maps, and study the SFR vs gas surface density relation directly. This investigation is one of the core science components of the Spitzer Infrared Nearby Galaxies Survey (SINGS; Kennicutt et al. 2003). The SINGS sample of 75 galaxies includes 24 objects from the BIMA SONG survey, and comparable resolution HI maps have been obtained at the Very Large Array (VLA) for a subset of SINGS spiral galaxies within 10 Mpc, as part of The HI Nearby Galaxy Survey (THINGS; Walter et al. 2005). The long-term goal is to combine SFR distributions of these galaxies derived from SINGS infrared and Hα imaging with the CO and HI maps to study the behavior of the star formation law down to scales of $6''$, the resolution of the Spitzer

24 μm, BIMA, and THINGS maps. This corresponds to linear scales of 0.1 – 0.5 kpc for most of the galaxies in the subsample.

In this paper we present the results of a pilot study of the spatially-resolved star formation law in the nearby spiral M51a (NGC 5194). This galaxy is ideal for a first study. It possesses a dense molecular disk with a high SFR per unit area, and a large variation in extinction ($A_V \sim 1 - 4$ mag), which allows us to test the efficacy of our extinction correction schemes. In addition, the galaxy has an especially rich multi-wavelength data set, including maps of the central disk in Paα (Scoville et al. 2001), which can be used to derive extinction-corrected local SFRs independently of the *Spitzer* observations, and thus quantify more accurately the uncertainties in the derived SFRs. The SINGS observations of this galaxy have been presented in an earlier paper (Calzetti et al. 2005; hereafter denoted Paper I). Following that paper we adopt a distance of 8.2 Mpc to M51.

The remainder of this paper is organized as follows. In §2 we describe the infrared, Hα, Paα, HI, and CO data that were used for this study, and in §3 we describe the methods used to extract local SFR and gas density measurements. Over much of the disk of M51 the intermediate levels of optical extinction introduce large errors into SFR measurements based either on Hα or infrared fluxes alone, and a combination of measurements is needed to provide reliable extinction-corrected SFRs. In §4 we describe a new method that we have devised to address this problem. In §5 we present the resulting SFR vs gas density relations, on varying linear scales and for the total gas density as well as for the atomic and molecular components considered individually. We also compare the spatially-resolved relation in M51 to the global SFR law found for galaxies in general. Finally in §6 we compare our results to theoretical expectations and explore their implications for modeling star formation in galaxies.

2. Data

The primary derived parameters for this study of the star formation law are local measurements of the SFR surface density and the atomic and molecular gas surface densities. We are interested in the instantaneous ($\tau < 5$ Myr) star formation, and have employed three tracers: Hα (0.66 μm) and Paα (1.87 μm) imaging to measure the ionization rate, and the 24 μm dust continuum imaging to trace the dust-obscured component of the star formation. Combinations of these are used to derive extinction-corrrected estimates of the SFR distribution. We have used a combination of CO maps from BIMA SONG and other published sources, along with 21-cm HI maps from the THINGS project to map the surface densities of molecular and atomic hydrogen, respectively. In this section we describe each of these data sets.

2.1. Spitzer Infrared Images

Spitzer MIPS observations of M51a at 24 μm were obtained on 22 and 23 June 2004, as part of the SINGS Legacy Program (Kennicutt et al. 2003). For this analysis we used the processed MIPS images from SINGS Data Release 4.[1] The reduction and mosaicing steps are described in Gordon et al. (2005) and Bendo et al. (2006). The final image mosaics have sizes $27' \times 60'$, fully covering M51a and the surrounding background. The 24 μm image traces the thermal dust emission from the galaxy. In Paper I we carried out a detailed comparison of the star formation in M51a as traced in Paα, 24 μm, and the ultraviolet, and we refer the reader to that paper for a detailed discussion of the datasets. In particular, Paper I revealed a very tight linear correlation between the Pα-derived ionizing fluxes of the HII regions in M51a and their 24 μm luminosities. In this paper we restrict most of our analysis of the Schmidt law to discrete infrared and emission-line sources, and consequently we will use the 24 μm fluxes exclusively as an infrared SFR tracer. Imaging with MIPS at 70 and 160 μm was obtained as part of the same observing campaign, but because of the low spatial resolution of those data ($\sim$18″ and 45″ FWHM, respectively) they were not used in this project.

The 24 μm map used for this paper is shown in Figure 1. It has a diffraction-limited resolution of 5.″7 FWHM and a 1-σ sensitivity limit of 1.1×10^{-6} Jy arcsec^{-2} for isolated sources. The point spread function (PSF) displays prominent Airy diffraction rings that limit the useful aperture sizes to approximately twice the FWHM beam width. The accuracy of the MIPS 24 μm photometric zeropoint is $\pm$5% (Engelbracht et al. 2007), although as discussed later, other factors limit the accuracy of most of our aperture fluxes to roughly $\pm$10% (also see Paper I).

2.2. Hα Emission-Line Images

Narrowband images centered at Hα and continuum R–band images were obtained on 28 March 2001, with the Cassegrain Focus CCD Imager on the 2.1–m telescope at Kitt Peak National Observatory, as part of the SINGS ancillary data program (Kennicutt et al. 2003). Two sets of exposures were taken to include the entire extents of M51a and its companion

[1]http://data.spitzer.caltech.edu/popular/sings

NGC 5195 in the images. Exposure times were 1800 s and 360 s per position for Hα and R, respectively. Standard reduction procedures were applied to the images.

Emission–line–only images were obtained by rescaling the R–band image and subtracting it from the narrow–band image. The narrowband filter used for the observation contains contributions from Hα as well as the neighboring [N II]$\lambda\lambda$6548,6583 forbidden lines. M51a has been the subject of numerous spectroscopic campaigns, and these data show an average [NII] excitation that is near the asymptotic value for metal-rich HII regions of [NII]λ6548,6583/Hα = 0.5 (e.g., Bresolin et al. 1999, 2004). We used this value to scale the image to net Hα surface brightness. In reality the [NII]/Hα ratio varies somewhat from region to region and as a function of radius in the galaxy, which introduces net flux errors across the image. Within the region covered by our CO data these variations introduce errors of $\sim$10% or less for most regions, and perhaps 20% in the most discrepant cases.

The final reduced Hα image used is shown in Figures 1 and 2. The accuracy of the absolute photometry was verified with an HST/WFPC2 Hα image of the center of the galaxy. The 1 σ sensitivity limit of our final Hα image is 1.8×10^{-17} erg s^{-1} cm^{-2} arcsec^{-2}. The measured PSF is 1.9″.

2.3. Paα Emission-Line Images

The Paα hydrogen recombination line at 1.87 μm provides a powerful probe of massive star formation even in relatively highly obscured regions (Quillen & Yukita 2001, Scoville et al. 2001). Likewise, the ratio of Paα to Hα flux provides a robust measurement of the nebular extinction. An extinction of 1 mag at V produces an extinction of 0.15 magnitudes at Paα, i.e., a small, $\sim$14% change in the line intensity. We adopt an intrinsic flux ratio Hα/Paα= 7.82 (Osterbrock & Ferland 2006), which applies to an assumed electron temperature of 7000 K and electron density of 100 cm^{-3} (Garnett et al. 2004, Bresolin et al. 2004). Extinction corrections were derived using the extinction curve of Cardelli et al. (1989), with k(Paα) = 0.455 and k(Hα)$-$k(Paα)=2.08, where the extinction curve is expressed in the form $I_{obs}(\lambda) = I_{intr}(\lambda)10^{[-0.4*E(B-V)*k(\lambda)]}$.

Archival HST/NICMOS images of the central 144″, corresponding to the inner $\sim$6 kpc of the galaxy, are available in the Paα emission line (1.8756 μm, F187N narrow–band filter) and the adjacent continuum (F190N narrow–band filter). The images form a 3$\times$3 NIC3 mosaic, and details of the observations, data reduction, and image mosaicing are given in Scoville et al. (2001). The nebular–emission–only image is obtained simply by subtracting the F190N from the F187N image, after rescaling for the ratio of the filter efficiencies. The NICMOS

PSF is undersampled by the NIC3 $0''.2$ pixels, and the average 1 σ sensitivity limit of the continuum–subtracted image is 1.8×10^{-16} erg s^{-1} cm^{-2} arcsec^{-2}, which is approximately an order of magnitude less sensitive than the Hα images, and another factor of eight lower when one considers the lower intrinsic brightness of Paα relative to Hα. However this is partly compensated for by the much lower extinction at Paα. Considering all these factors together the effective sensitivity of the Paα image to a fixed SFR per unit area is roughly a factor of ten lower than that of the Hα image, so its use is limited to the brightest HII regions in the inner disk. Nevertheless it is critical for providing a calibration for the other extinction correction methods used in this paper.

2.4. Radio Continuum Fluxes

Multi-frequency radio continuum fluxes are available for 43 bright HII regions in M51a from the study of van der Hulst et al. (1988). This study was based on aperture synthesis maps at wavelengths of 6 cm and 20 cm made with the Very Large Array (VLA), with matching resolutions of $8''$. The two-frequency observations allowed these authors to make a rough separation of non-thermal and thermal radio fluxes. The thermal bremsstrahlung luminosities provide independent measures of the extinction-corrected ionizing fluxes for the HII regions, and when combined with Hα fluxes independent estimates of the visible extinction. A full description of these measurements can be found in van der Hulst et al. (1988).

2.5. VLA HI Observations

HI data for M51a have been obtained through The HI Nearby Galaxy Survey (THINGS), a survey dedicated to obtain high-resolution VLA HI imaging for $\sim$35 nearby galaxies (Walter et al. 2005). M51 was observed in the VLA D (9 July 2004), C (26 April 2004) and B array (05 March 2005) configurations for 80, 120, and 390 minutes on source, respectively (or a total of $\sim$ 10 hours on source). The calibration and data reduction was performed using the AIPS package[2]. The absolute flux scale was determined by observing 3C286 in all observing runs (using the flux scale of Baars et al. 1977). The same calibrator was used to derive the bandpass correction. The time variable phase and amplitude calibration was performed using the nearby, secondary calibrators 1313+549 and 1252+565 which are unresolved for the arrays used. The *uv* data were inspected for each array, and bad data points due to either

[2]The Astronomical Image Processing System (AIPS) has been developed by the NRAO.

interference or crosstalk between antennae were removed. After final editing and calibration, the data were combined to form a single dataset and maps.

In order to remove the continuum we first determined the line-free channels in our observation and subtracted the continuum emission in the *uv* plane. Datacubes (1024 × 1024 pixels × 80 channels each) were produced using the task IMAGR in AIPS. To obtain the best compromise between angular resolution and signal/noise, we used a ROBUST parameter of 0.5 for the final imaging. This led to a resolution of 5.″82 × 5.″56, and an rms of 0.44 mJy beam^{-1} in a 5.2 km s^{-1} channel. The correspoding 3σ sensitivity for the integrated map is 1.6×10^{20} cm^{-2} (corresponding to 1.3 M$_\odot$ pc^{-2}). To separate real emission from noise for the final integrated HI map (moment 0), we considered only those regions which showed emission in three consecutive channels above a set level ($\sim 2\sigma$) in datacubes convolved to 330″ resolution. The final corrected HI image is shown in Figure 1.

The fluxes in the integrated HI map are corrected for the fact that typically the residual flux in cleaned channel maps is overestimated (sometimes severely) due to the different shapes of the dirty and cleaned beams (see e.g., Jorsater & van Moorsel 1995, Walter & Brinks 1999). With these corrections taken into account we estimate our column densities to be correct within ±10%.

2.6. BIMA SONG CO Observations

The CO J=1–0 map of M51a was obtained as part of the BIMA Survey Of Nearby Galaxies (BIMA SONG), and details on the data taking and processing can be found in Helfer et al. (2003). The map used in the analysis is shown in Figure 1. The interferometric BIMA data on M51 were combined with single dish data obtained at the former NRAO 12 m telescope using on-the-fly mapping. In total, a 26 pointing mosaic was observed with BIMA in the C and D configurations, leading to a beamsize of 5.″8 × 5.″1 (i.e., matched to the HI data) and a velocity resolution of 4 km s^{-1} (similar to the HI observations). The map covers the central ∼350″, or ∼13.8 kpc of the galaxy. The rms sensitivity in a 10 km s^{-1} channel is 61 mJy beam^{-1}. The corresponding 3σ sensitivity for the BIMA SONG map is ∼13 M$_\odot$ pc^{-2} (Helfer et al. 2003). This is considerably higher than the corresponding HI surface density limit; the limiting sensitivity of our cold gas surface density measurements is set by the CO data.

Molecular hydrogen column densities were calculated from the CO map, using the conversion of Bloemen et al. (1986): $N(H_2) = 2.8 \times 10^{20}\ I_{CO}$ cm^{-2} (K km s^{-1})$^{-1}$. The high metallicity and small metallicity range in the disk of this galaxy (Bresolin et al. 2004) justifies the use of a single conversion factor. Our choice of the Bloemen et al. conversion factor is somewhat arbitrary and was done in part to maintain consistency with the Schmidt law study of Kennicutt (1998b). Moreover this value lies in an intermediate range between lower factors derived by Strong et al. (1988) and Hunter et al. (1997) and higher values by Blitz et al. (2007) and Draine et al. (2007) ($1.56 - 4.0 \times 10^{20}$ cm^{-2} (K km s^{-1})$^{-1}$). As will be shown in §5.1, the choice of conversion factor mainly affects only the zeropoint of the Schmidt law and not its form, because molecular gas is dominant over the atomic component in the regions studied here, to such a degree that the inferred total gas densities scale almost linearly with the CO conversion factor used.

2.7. FCRAO CO Data

Single-dish CO maps covering the central 310″ of M51a with a beam size of 45″ HPBW (1850 pc at the adopted distance) are also available from the study of Lord & Young (1990). The advantage of these data is that they provide fuller spatial sampling of the disk (the sensitivity of the BIMA SONG maps only allows us to measure CO intensities reliably in high surface brightness peaks), and thus they allow us to check whether the form of the Schmidt law changes significantly when the spatial scales probed are increased from 300 pc to 2 kpc. As before, we have used the Bloemen et al. (1986) conversion factor to calculate molecular hydrogen column densities from the published CO fluxes.

2.8. Total Gas Densities

With the conversion factors given above, molecular gas dominates over the atomic component at most positions in the disk of M51a (Scoville & Young 1983, Lord & Young 1990). However since most previous studies of the Schmidt law have been parametrized in terms of the total gas surface density we computed total hydrogen column densities at most positions. These in turn were converted to gas mass surface densities assuming:

$$\Sigma_H \;\; (M_\odot \; pc^{-2}) = ((N_{HI} + 2N_{H_2})/(1.25 \times 10^{20} \; cm^{-2}). \qquad (3)$$

In order to maintain consistency with Kennicutt (1998b) we parametrized the gas surface density in terms of hydrogen surface density alone. Total gas surface densities, including helium and metals, would be larger by a factor of $\sim$1.36, depending on the metallicity and dust depletion factor adopted.

3. Measurement of Local SFRs and Gas Densities

3.1. General Considerations

Before we describe the local flux measurements and attempt to interpret the correlations we find it is useful to examine qualitatively the behavior of the gas and star formation distributions. These are illustrated in Figure 1, which shows four of the maps that were used for the main part of the analysis: Spitzer 24 μm, Hα (KPNO), VLA HI, and BIMA SONG CO maps.

Figure 1 shows that all of the gas and star formation tracers follow qualitatively similar spatial distributions. The strong tidal interaction with NGC 5195 has organized the cold gas into strong and relatively narrow spiral arms, and the star formation closely follows this structure. Within the inner disk the gas is predominantly (>90%) molecular, with HI dominating only outside of the main star-forming disk (Lord & Young 1990). This gas disk is dense, and the bulk of the massive star formation is taking place in very massive cloud complexes and giant HII regions. When averaged over our primary aperture size ($13'' =$ 520 pc, see §3.2), typical cloud complexes have surface densities of order 10–1000 M$_\odot$ pc^{-2} ($N_H \sim 10^{22} - 10^{24}$ H cm^{-2}), and gas masses within these apertures of order 2×10^6 – 2×10^8 M$_\odot$. Likewise the extinction-corrected ionizing fluxes of the regions range over $\sim 10^{49} - 10^{51}$ photons s^{-1}, comparable to the 30 Doradus complex in the Large Magellanic Cloud (e.g., Kennicutt 1984). Consequently the nebular ionization is provided by clusters and associations of order tens to thousands of O-stars. The unusual strength of the dynamical disturbance and response of the gas disk in M51a offers both advantages and disadvantages for this study. Few nearby galaxies contain such a large number of massive and dense star-forming complexes, and this allows us to characterize the star formation law with more than 200 regions. On the other hand the combination of the strong concentration of star formation in spiral arms with the finite sensitivity limits of our CO data restrict us to characterizing the behavior of the law in a high-density and high-SFR regime, above the level where cloud formation and/or star formation thresholds may become important.

Generally speaking there is spatial correspondence between the locations of peaks in the cold gas components and star forming regions (see Figure 1d of Aalto et al. 1999). Upon close examination some subtle differences can be seen, such as a shift between maxima in the CO and HI distributions, as discussed by Tilanus et al. (1988). These displacements were interpreted by those authors as evidence that the HI is formed by photodissociation of the molecular gas by hot stars located even farther downstream in the spiral pattern. Similar downstream offsets between the locations of the star formation peaks (as traced at Hα, Paα, and 24 μm) and the CO peaks are also observed at times (also see Aalto et al. 1999), but a detailed analysis of this lies beyond the scope of the current study. These displacements can be relevant to quantifying the form of the star formation law, by imposing a limiting spatial scale over which we can make this comparison. Fortunately the youngest star forming clusters traced in Hα, Paα, and 24 μm have not drifted significantly away from their natal clouds, and we can reasonably study the SFR density vs gas density correlation on scales down to $\leq$200 pc. However, as shown later the beam sizes and profiles of our MIPS and CO/HI data impose a minimum aperture diameter of about 500 pc (12$''\!.$6 at the distance of M51a) anyway. This scale is of prime interest for galaxy evolution modeling and understanding the large-scale initiation and regulation of star formation.

When examined on these larger scales, we find an almost one-to-one correlation between the locations of gas peaks and star formation events. For example we were able to identify only 2 significant CO peaks in the BIMA SONG map (out of 257 regions studied) that do not show well-detected star formation in the visible and/or infrared. The positions of these two clouds are highlighted by magenta circles in an Hα map shown in Figure 2. Comparison with the CO map in Figure 1 shows that they are prominent CO peaks, with surface densities of $\sim$250 M$_\odot$ pc^{-2} or total molecular masses of order 5×10^7 M$_\odot$, and are among the largest clouds in the galaxy. Both are located at the inside edge of the southern spiral arm, which is at least qualitatively consistent with them being young clouds. We find no significant emission features at these positions in any of our other emission-line or Spitzer maps; examination of the high-resolution HST images reveals the presence of a large dust feature coincident with the southern cloud in the pair. We tentatively conclude that these are very young clouds that have yet to undergo significant massive star formation, though we reiterate that such clouds are very rare in M51a, comprising fewer than 1% of the regions studied. This suggests a relatively short timescale for the onset of star formation relative to the lifetimes of the molecular concentrations, at least under the (relatively extreme) conditions present in M51 today. As a practical matter this result simplifies our analysis, because it means that the form of the derived star formation law will not be sensitive to the method used to select the measuring apertures.

3.2. Aperture Photometry and Local Flux Measurements

Our analysis of the star formation law in M51a is based on aperture photometry in Paα, Hα, and 24 μm (to determine local SFRs), and in CO and HI (for gas densities). The primary dataset is based on measurements made with 13$''$ diameter apertures, which corresponds to a physical diameter of 520 pc at the distance of M51. This aperture size is mainly dictated by the point spread function of the *Spitzer* 24 μm images.

Ideally one would measure the correlation between SFR and gas surface densities by applying apertures at every position in the disk. Unfortunately our data are not sufficiently sensitive to permit this completely unbiased characterization of the star formation law. Because of the limited depth of the CO maps, reliable gas surface densities can only be measured in apertures that cover of order 10% of the area of the star-forming disk. If we were to "measure" gas and SFR surface densities at every point in the disk, ∼90% of the data points would be upper limits in both axes, and any correlations revealed by these data would be physically meaningless. With these limitations in mind we adopted a two-part strategy. To characterize the star formation law on the smallest scales available to us we analyzed 13″ aperture photometry restricted to 257 positions (below) where star formation was detected (§5.1). Then to provide a comparison set of (nearly) spatially complete measurements, we used the 45″ single-dish CO data of Lord & Young (1990) with matching infrared and Hα aperture photometry (§5.2).

The aperture positions for the 13″ measurements are shown in Figure 2. Centers were selected to coincide with 24 μm and Hα emission peaks, yielding a total of 257 positions. In Figure 2 red circles indicate positions where significant flux was detected in HI and CO, while blue circles indicate positions where we could only measure an upper limit in CO; this is discussed in more detail in §5.1. The two magenta circles mark the positions of CO concentrations without Hα or infrared sources, as discussed earlier.

The photometric apertures were applied with a minimum separation of centers of 7.″5 in the crowded central regions where Paα was measured, and with minimum separations of 13″ elsewhere. This was imposed to minimize the contamination from neighboring apertures in cases where the 24 μm emission was used in conjunction with Hα for deriving SFRs. In particular, the MIPS 24 μm PSF gives contamination levels of ∼5% for an aperture centered 13″ away (Calzetti et al. 2005). The use of 13″ apertures also required the application of aperture corrections to the 24 μm fluxes; we used a point-source correction factor of 1.67 (Engelbracht et al. 2007). Aperture corrections were not needed for data taken at other wavelengths. For a few positions in the central disk the separation between sources is less than the aperture diameter, producing overlapping apertures; however only 8 of the 257 regions were affected by this problem.

The need for relatively large measuring apertures introduces considerable background contamination of the aperture fluxes in the Hα, Paα, and 24 μm measurements, from neighboring regions and diffuse background. This contamination is strongest in the 24 μm maps, which contain an extended background component that is probably produced in large part by dust heated by older stars (e.g., Popescu & Tuffs 2002, Gordon et al. 2004). This diffuse component contributes 15–34% of the total 24 μm luminosity of M51, depending precisely on how the separation between point sources and diffuse background is made (Paper I, Dale et al. 2007). Conventional background subtraction using annular regions around the apertures could not be used here, because of contamination with neighboring regions in many cases. Instead we adopted the same strategy as used in Paper I for local background removal. We identified 12 rectangular areas, each encompassing a fraction of the 257 apertures, and fitted the local background in each of these regions. Figure 2 shows the locations of these background rectangles. The net effect of subtracting backgrounds is to reduce slightly the dispersion in the observed star formation laws, but the best-fitting Schmidt laws are virtually identical regardless of whether backgrounds are subtracted or not. Background removal was not necessary for the HI and CO maps.

A similar process was used to measure 24 μm, Hα and HI fluxes for 45″ apertures matching the published CO measurements of Lord & Young (1990). In this case the positions of the apertures were pre-determined by the CO measurements. Background corrections were applied to the Hα and 24 μm data to maintain consistency with analysis described above.

Measurement uncertainties assigned to the photometric values are a quadratic sum of four contributions: random measurement uncertainties in the raw source fluxes, variance of the local background (from the original–pixel–size images), photometric calibration uncertainties (5% for Paα, Hα, and MIPS 24 μm), and variations from potential mis-registration of the multiwavelength images (at the level of 1″.5). For the determination of gas surface densities the dominant error term for most objects is measurement uncertainty in the CO flux. Conservative uncertainty estimates were employed on the CO map to discriminate detections from upper limits. Such conservative estimates were produced by quadratically combining the formal standard deviation with the dispersion of multiple measurements obtained within a radius of 13 arcseconds (twice our fiducial measurements radius) in low signal–to–noise regions. For the SFR surface densities the relative uncertainties usually are much lower, and are dominated by the source flux and/or background and crowding terms.

The flux measurements in this paper are compiled in machine-readable form in Table 1. This includes positions for the 13″ HII region measurements and the 45″ areal photometry, for Hα, Paα (when available), 24 μm, as well as HI and H_2 column densities derived from the radio maps. We also compile the derived, extinction-corrected SFR surface densities and total hydrogen gas densities, as described in the next section.

4. A New Combined Hα + Infrared SFR Measure

Any study of the spatially-resolved star formation in M51a must contend with the substantial and locally variable dust extinction (e.g., Scoville et al. 2001). The median attenuation of the M51a HII regions is about 2 mag at Hα, with a range of 0–4 mag among individual objects (Paper I). This means that neither Hα nor 24 μm fluxes by themselves provides reliable extinction-corrected SFRs across the disk. Dust extinction clearly will cause the Hα fluxes to underestimate the SFRs in most regions, often severely, while the infrared fluxes by themselves will also underestimate the SFRs in the regions with low to moderate extinction.

In the center of the galaxy ($R \leq 72'' = 3$ kpc) we have Paα imaging, and the combination of Paα and Hα photometry allows us to derive robust extinction corrections (the average extinction of the HII regions at the wavelength of Paα is only ∼0.4 mag). However Paα data are not available for most of the disk of M51a, and even where they are available they can only be applied to 77 high surface brightness regions. This effectively imposes a limiting SFR surface density of ∼0.05 $M_\odot$ yr^{-1} kpc^{-2}, only ∼10 times lower than the maximum observed SFR density, and insufficient to reliably define the form of the Schmidt law. Therefore in order to extend the range of SFR densities probed we need a second extinction-corrected SFR measure that does not rely on Paα data.

In principle it should be possible to combine the observed (extincted) Hα fluxes with the infrared fluxes to derive extinction-corrected emission-line luminosities, because the infrared emission comprises most of the stellar luminosity that was attenuated by the dust. A variant of this approach was introduced by Gordon et al. (2000) as the "flux ratio method," in which they used the combination of ultraviolet and infrared fluxes of galaxies to derive extinction-corrected UV luminosities and SFRs (also see Bell 2003, Hirashita et al. 2003, and Iglesias-Paramo et al. 2006). Here we introduce a similar method, but one which combines measurements at Hα and 24 μm to derive extinction-corrected Hα and ionizing luminosities.

The basis for this method is the observation in Paper I of a very tight and linear correlation between 24 μm and extinction-corrected Paα luminosities for 42 dusty HII regions in the center of M51a (where 80–90% of the total stellar luminosity is reradiated in the infrared). Subsequent work has shown that this trend extends to other highly-extincted HII regions in other galaxies (Wu et al. 2005; Alonso-Herrero et al. 2006; Calzetti et al. 2007). This correlation allows us to empirically calibrate a relation between 24 μm luminosity and the SFR that is directly tied into the Hα (or Paα) based scale. A tight linear scaling between ionizing flux and 24 μm flux might be expected if single-photon heating of small dust grains (<50 Å in radius) dominates the emission in this wavelength range, or if the average temperature of the emitting dust does not vary substantially from position to position.

Following the precepts of Gordon et al. (2000) we can parametrize the Hα attenuation in terms of a simple energy balance. To a first approximation the amount of extincted Hα radiation should scale with the luminosity re-radiated in the infrared:

$$L(H\alpha)_{corr} = L(H\alpha)_{obs} + a\ L(24) \tag{4}$$

where $L(H\alpha)_{obs}$ and $L(H\alpha)_{corr}$ refer to the observed and attenuation-corrected Hα luminosities, respectively, $L(24)$ is defined as the product νL_ν at 24 μm, and a is the scaling relation that is fitted empirically, using independently extinction-corrected data such as Paα and Hα measurements. The same relation can be used to measure the effective Hα attenuation:

$$A(H\alpha) = -2.5 \log \frac{L(H\alpha)_{obs}}{L(H\alpha)_{corr}} = 2.5 \log{(1 + \frac{a\ L(24)}{L(H\alpha)_{obs}})} \tag{5}$$

Note that in the limit of zero extinction the infrared term vanishes, and $L(H\alpha)_{corr} = L(H\alpha)_{obs}$. In the opposite limit of very high extinction, $L(H\alpha)_{obs}$ vanishes and $L(H\alpha)_{corr} = aL(24)$. This defines the scaling constant a.

The relations in eqs. (4−5) are empirical approximations to a much more complicated extinction geometry in individual regions. In a real HII region the ratio of observed Hα luminosity to infrared luminosity will depend on the dust optical depths and geometry, which will influence the amounts of extinction and the energy distribution of the emitting dust, and on the spectral energy distributions of the embedded stars, which affect the ratio of ionizing to dust heating radiation. All of these factors will vary from object to object and introduce a scatter into the relations between actual Hα extinctions and the values estimated from eq. (5). Our interest is in applying these relations statistically, and we can use the observed scatter against independently determined luminosities and extinctions to constrain the reliability of the results.

In M51a we have independent extinction-corrected Hα luminosities for 42 HII regions from the Paα measurements, and we used these to calibrate the mean value of a in equation (4). The results are shown in the left panel of Figure 3. There we compare the extinction-corrected Hα luminosities of the HII regions derived from the observed Hα fluxes, 24 μm fluxes, and eq. (4) with extinction-corrected Hα luminosities of the same objects as derived from the ratio of Paα/Hα (abscissa). We find a best fit for a L(24)/L(Hα) scaling constant $a = 0.038 \pm 0.005$. The rms dispersion of the individual regions about the mean relation is ± 0.1 dex ($\pm 25\%$), which provides an empirical estimate of the accuracy of the attenuation corrected luminosities. The scatter reflects a combination of measuring uncertainties in the Paα and 24 μm fluxes, along with errors in the application of equation (4) caused by variations in cluster age, dust geometry, etc. In the righthand panel of Figure 3 we compare the corresponding V-band attenuations derived using the two methods. The average scales are constrained to be the same, because we calibrated the coefficient in eq. (5) using these regions; the main result of interest is the dispersion of points about the mean relation ($\pm$0.25 mag). This can be compared to the systematic errors that would be introduced if no extinction correction were applied, 1–3.5 mag (factor 2–25) for these regions.

We can also compare our extinction-correction values and luminosities to those derived from a comparison of thermal radio continuum and Hα fluxes by van der Hulst et al. (1988). Those authors used 6 cm and 20 cm VLA maps of M51 to perform an approximate separation of thermal (free-free) and non-thermal (synchrotron) components to the fluxes. The thermal radio fluxes scale linearly with the ionizing fluxes, with a mild dependence on electron temperature (assumed to be 7000 K). Estimated thermal radio fluxes at 6 cm are available for 32 HII regions in common with our sample. The resulting luminosities for individual regions have larger uncertainties than those derived from Paα, because of the lower signal/noise of the radio data and uncertainties in the corrections for nonthermal emission, typically $\pm$20–50% (van der Hulst et al. 1988). However the data provide a valuable check on the overall extinction and corrected flux scales. The median radio-derived attenuation for the 32 HII regions is A(Hα) = 1.9 mag, which is similar to the median value of 1.75 mag using eq. (5). In view of the considerable uncertainties in the radio data (typically $\pm$0.5 mag in derived extinction at Hα) we regard this as reasonable consistency. We defer further discussion of this method to a more extensive analysis by Calzetti et al. (2007), which incorporates Paα, Hα, and 24 μm measurements of 220 HII regions in 33 galaxies, and reinforces the conclusions drawn above.[3] In that paper we also show that the empirically determined value of a in eqs. (4−5) is consistent with expectations from simple evolutionary synthesis models of young star clusters surrounded by gas and dust.

In the remainder of this paper we use equation (4) to estimate Hα extinction corrections for the 215 HII regions in M51a that were not measured in Paα (and the 42 regions with Paα data as well). We hasten to emphasize however that our calibration of a is based on and tailored to the HII regions in M51a, and may not necessarily apply in all physical situations. In particular our determination of the scaling factor a for HII regions cannot be applied

[3]The best fitting value of the calibration constant derived in the Calzetti et al. analysis is slightly different, $a = 0.031$ *vs* 0.038 derived here. For this analysis we have opted to use the latter value, since it was derived from the same data that are used to measure the SFRs in M51a. However adopting the other value of a would not alter the results presented in this paper significantly.

to galaxies as a whole, because galaxies contain a significant component of 24 μm dust emission that is not associated with HII regions. The application of this method to galaxies is addressed in a separate paper (Kennicutt & Moustakas 2007, in preparation). Likewise one would expect the method to break down badly in small HII regions that are predominantly ionized by single stars, because in such regions the ratio of ionizing luminosity to dust-heating luminosity will be strong functions of ionizing stellar type, age, and the cluster mass function. These will vary enormously (and systematically) from object to object.

5. Results: The Local SFR Density vs Gas Density Relation

The measurements described in the previous section provided us with extinction corrected emission-line fluxes for the 257 star-forming regions in the area covered by the BIMA SONG map. These include Paα measurements for 77 regions in the central 144$''$ (corrected for dust attenuation via Paα/Hα) and 24 μm + Hα fluxes for 180 regions (these include 25 objects in the inner 144$''$ region that were not detected in Paα).

Up to now we have measured ionizing fluxes of HII regions and their embedded OB associations, and we now would like to transform these to equivalent SFRs and SFRs per unit area. For HII regions with sufficiently high luminosity (($L_{corr}(H\alpha) \geq 10^{39}$ ergs s^{-1}, ionizing photon flux $Q(H^0) \geq 10^{51}$ s^{-1}), the ionizing star clusters need to be sufficiently massive such that their initial mass functions will be well populated to high masses, and we can safely assume that the ionizing fluxes (at fixed age) will scale roughly with the total stellar masses of the clusters (e.g., Kennicutt 1988, Cerviño et al. 2002) and thus the SFR. With this in mind we have converted the line fluxes into equivalent SFRs, using the calibration of Kennicutt (1998a) that is usually applied to galaxies as a whole.

$$SFR\ (M_\odot\ yr^{-1}) = 7.9 \times 10^{-42}\ L_{corr}(H\alpha)\ \ (ergs\ s^{-1}) \tag{6}$$

This conversion assumes a Salpeter IMF over the range of stellar masses 0.1 − 100 M$_\odot$. We caution that a "star formation rate" derived in this way for an individual HII region, using a continuous star formation conversion relevant to entire galaxies, has limited physical meaning, because the stars are younger and the region under examination is experiencing an instantaneous event when considered on any galactic evolutionary or dynamical timescale. One must also bear in mind that age differences among the HII regions will change the actual ratio of ionizing flux to stellar mass, and thus introduce scatter into the derived Schmidt law. However for this analysis we are mainly interested in the shape of the star formation law, and the normalization of the SFR scale is somewhat arbitrary. Adopting a global conversion provides a convenient standard and will also allow us to compare the form and zeropoint of the relation with that measured for galaxies as a whole; this is discussed in the next section.

In order to cast these measurements in the form of a Schmidt law, the SFRs then need to be converted to SFR surface densities by normalizing the rates to an appropriate area. We followed the most straightforward approach of dividing the SFR by the projected area of the 13″ apertures, and divided by an additional factor of 1.07 to correct for the 20° inclination of M51a (Tully 1974). The gas surface densities were corrected by the same projection factor. This choice of normalization is somewhat arbitrary, but we believe it is the most physically meaningful choice, because it corresponds to the approximate size of the emitting regions, their associated gas complexes, and to the sizes of the regions measured. Note that the power law exponent of the derived Schmidt law derived form is insensitive to the apertures used; adopting a larger aperture, for example, will simply decrease the measured gas and SFR surface densities by the same beam dilution factor for most points. This shift however will change the zeropoint constant of the derived Schmidt law (discussed in more detail in §5.3).

5.1. The Star Formation Law on 500 Parsec Scales

One of the main results of our paper is summarized in Figure 4, which shows the relationship between the SFR and gas surface densities for the 257 regions covered by the BIMA SONG map, measured with apertures of 13″ (520 pc) diameter. Solid triangles denote SFRs measured from Paα, while open triangles show those with SFRs determined from 24 μm and Hα measurements. For the sake of clarity we have removed the error bars in the right panel, while the same data with error bars are shown in the left panel. Open circles in the righthand panel denote positions where we only could determine an upper limit to the CO flux; for those we plot the HI surface density as a lower limit and the sum of the 1σ H_2 surface density plus the HI surface density as an upper limit. The SFRs and gas surface densities are strongly correlated, and follow a roughly power law relation in the mean. The solid line in both plots shows a bivariate least square fit:

$$\log \Sigma_{SFR} = (1.56 \pm 0.04)\ \log \Sigma_H - (4.32 \pm 0.09) \tag{7}$$

where the SFR surface density Σ_{SFR} is expressed in units of $M_\odot\,yr^{-1}\,kpc^{-2}$ and the hydrogen gas surface density Σ_H is expressed in units of $M_\odot\,pc^{-2}$. The uncertainties given in the equation refer to random fitting errors only. Some of the data points shown in Figure 4 carry large uncertainty estimates in the gas surface densities (left panel), and this may give rise to concerns about the robustness of the fit given above. We tested this by refitting the data with 25 interarm regions with large uncertainties in CO fluxes removed. The resulting relation ($\log \Sigma_{SFR} = (1.57 \pm 0.05)\ \log \Sigma_H - (4.36 \pm 0.09)$) is the same within the formal errors, so this does not appear to be a serious concern.

The scatter in the correlation is significant, with an rms dispersion about the best fit of ± 0.4 dex. This is comparable to the dispersion in the global Schmidt law relation of Kennicutt (1998b). Fortunately M51a offers a large dynamic range in local SFR and gas surface densities (factors of roughly 1000 and 100, respectively), so the correlation is well defined despite this large point-to-point scatter.

What are the likely sources of this dispersion, and does any of it reflect a real physical variation? As indicated by the error bars in the left panel of Figure 4, observational uncertainties in the gas masses are the dominant source of error at low surface density, below $\sim$20 $M_\odot$ pc^{-2} or about $2 - 3 \times 10^{21}$ cm^{-2} in column density. As a result our observations do not offer much insight into the physical nature of the scatter below those densities, or for star formation surface densities below about 0.01 $M_\odot$ yr^{-1} kpc^{-2}; observations of other galaxies in the future should reveal more about that surface density regime. However it is clear that at least some of the dispersion in the Schmidt law above these scales is physical. This is best seen at the upper surface-density end of the plot, where the scatter clearly is larger than the random observational errors, and is much larger than the random uncertainties in the extinction-corrected luminosities ($\pm$ 0.1 dex, see Fig. 3). There are a number of possible causes for this large scatter. Variations in the ages of the regions must be a factor; as a molecular complex evolves the ionizing flux will first peak then dissipate, and the cold gas mass of the complex will evolve as well, as the region disperses over time. Moreover we have no reason to expect *a priori* that the conversion fraction of gas to stars is a universal constant in all clouds (see discussion in §6).

None of the mechanisms discussed above are likely to bias the slope of the SFR surface density vs gas surface density law to a significant degree. Another parameter that might influence the dispersion or even the slope of the measured Schmidt law would be a large variation in the CO/H_2 conversion factor X. A fixed value of X has been adopted in this analysis. The conversion factor would need to fluctuate by nearly an order of magnitude to account for the observed scatter, and this is unlikely. A multi-frequency study of M51a in CO by Garcia-Burillo et al. (1993) found evidence for possible variations in X between the spiral arm and interarm regions, so we cannot rule out some possible bias due to CO/H_2 variations. However we suspect that the dispersion mainly arises from a combination of measuring uncertainties (especially in the molecular gas surface densities) and physical effects including variations in the ages of the associations and clusters and actual variations in the star formation efficiency among the clouds.

Figure 5 shows the correlation with the HI and inferred H_2 surface densities separately. Molecular gas dominates most of the gas clouds in the inner disk of M51a, so the comparison of SFR and H_2 surface densities is similar to the relation in Figure 4:

$$\log \Sigma_{SFR} = (1.37 \pm 0.03)\ \log \Sigma_{H_2} - (3.78 \pm 0.09) \tag{8}$$

where the units for the SFR and hydrogen surface densities are the same as in eq. (7). The slope of this molecular-only relation is significantly shallower than for the SFR vs total (atomic + molecular) surface density relation ($N = 1.37 \pm 0.03$ vs 1.56 ± 0.04); this arises because the atomic gas contribution is proportionally larger in the lowest surface density regions.

The strong correlation observed between the local SFR surface densities and molecular gas surface densities in M51a is quite unlike the relatively poor correlation between the disk-averaged SFRs and molecular surface densities of normal spiral galaxies (e.g., Buat et al. 1989, Kennicutt 1989). However our result is consistent with other spatially-resolved measurements of nearby galaxies, based on either point-by-point measurements of azimuthally averaged radial profiles of SFR and gas surface densities (Kennicutt 1989, Wong & Blitz 2002, Heyer et al. 2004, Komugi et al. 2005). These studies yielded power law exponents N between 1.3 and 1.4 when the SFR and molecular gas surface densities are correlated. Likewise Zhang et al. (2001) derive N = 1.20–1.38 from an analysis of star-forming regions in the Antennae (NGC 4038/9); their fits apply to the total gas surface density, but since most of the regions are dominated by molecular gas this is consistent with the other results cited here. Two other papers report different results. Kuno et al. (1995) carried out a point-by-point analysis of M51a using $16''$ beam CO observations with the Nobeyama Radio Observatory along with published CO and Hα data. They derived a best-fitting Schmidt law slope $N = 0.7 \pm 0.1$. The different result can be attributed the adoption of a much lower CO/H_2 conversion factor in the Kuno et al. study (1.0×10^{20} *vs* 2.8×10^{20} $H_2\,(\mathrm{K\,km\,s^{-1}})^{-1}$ here), which is low enough for HI to be the dominant component in many regions, and the absence of any extinction corrections in the (Hα) SFR measurements. An analysis of radial profiles of 11 nearby spirals by Boissier et al. (2003) derived significantly steeper ($N \sim 2$) Schmidt law indices; the difference in this case can be attributed to their use of a radially varying (metallicity-dependent) CO/H_2 conversion factor (a constant factor was used in the other studies cited). These comparisons underscore the dominant role of systematic uncertainties such as the CO/H_2 conversion factor and accurate extinction corrections in determining the form of the observed SFR vs gas surface density relation in galaxies.

In contrast to the strong correlation seen in Figure 5 between the SFR and molecular gas surface densities, there is virtually no correlation between the local SFR surface density and the HI surface density. We found this somewhat surprising, because if the HI is formed by the photodissociation of molecular gas by ambient stellar ultraviolet radiation (e.g., Shaya & Federman 1987, Tilanus & Allen 1991), one might expect the atomic surface density to scale with the local SFR density (Allen et al. 1997). In any case the lack of any clear correlation between SFR surface density and HI surface density on local scales stands in stark contrast to the relatively strong SFR vs HI correlation seen on global scales in disks (e.g., Buat et al. 1989, Kennicutt 1989). This difference probably arises in part from the different molecular fractions in the two cases. Molecular gas comprises >90% of the cold gas in M51a, and is even more dominant in the center of the galaxy (Lord & Young 1990), so there HI is a trace species, especially in the dense peaks where star formation takes place. On the other hand HI typically comprises ∼50% of the cold gas in the disks of the spirals studied by Kennicutt (1989, 1998b), and the objects studied have a much larger range of SFRs and metallicities. Nevertheless the poor correlation between SFR and HI surface densities in Figure 5 raises the interesting question of whether the global correlation breaks down generally on subkiloparsec scales. This is a question we intend to pursue with studies of the larger SINGS sample.

Another interesting feature in Figure 5 is the presence of an apparent upper limit to HI surface density, at about 25 $M_\odot$ pc^{-2}, or a corresponding HI column density of $\sim 2 \times 10^{21}$ cm^{-2}. Inspection of the HI map shows that this is a general characteristic of the disk; a histogram of column densities shows a sharp falloff above this value. A similar behavior was seen by Wong & Blitz (2002) in an analysis of radial profiles of HI, CO, and Hα for a subset of BIMA SONG galaxies. We suspect that this represents the column density above which conditions in the clouds strongly favor the formation of a dominant molecular medium. Since most of the star formation in M51a takes place in denser molecular-dominated regions perhaps the lack of correlation between SFR density and HI surface density should not be surprising.

The upper envelope of the SFR surface density vs gas surface density correlation tends to be dominated by regions with relatively weak CO emission. This is shown clearly in the right panel of Figure 4, where circles denote the positions of CO (3σ) upper limits. Many of these regions are also faint in HI, Hα, and the infrared, and may be nothing more than small star forming clouds that fall just below the detection limits of the BIMA CO map. Some of these could be evolved clouds, where star formation is well established and the parent molecular clouds are dissipating. This latter interpretation is supported somewhat by the spatial distribution of the upper limit points. As can be seen in Figure 2, the regions with CO upper limits (blue circles) preferentially lie outside of the main spiral arms. However roughly a third of the points coincide with or lie inside the main Hα arms, so this evolutionary hypothesis cannot be the sole explanation. Otherwise we did not detect any systematic dependence of the Schmidt law zeropoint on arm position, but this is hardly surprising in view of the observational uncertainties in the gas surface densities.

Finally, Figure 6 shows the same data as plotted in Figure 4, but here with the points coded in color by galactocentric radius. This is useful for checking whether the Schmidt law itself could be dependent on radius, and also whether there are any hints of other radially dependent systematic effects in the data. The comparison shows that the Schmidt laws at different radii largely overlap with each other; there is no evidence for any significant radial dependence. The only possible exception is the strong clustering of points at high SFR and gas density at the very smallest radii (0.5–2 kpc), where there is a hint of a turnover in the power law. This could arise from a number of measurement effects, such as a change in the CO/H_2 conversion factor at the highest metallicities or a significant absorption of ionizing photons by dust in the dustiest central regions, or from a physical effect, as introduced for example by a change in disk kinematics in the central regions.

5.2. The Star Formation Law on Other Linear Scales

It is interesting to examine whether the form of the star formation law changes significantly as a function of the physical scale over which the SFRs and gas densities are correlated. Here we combine our data with other single-dish studies to explore such variations on scales of $\sim$0.3 − 1.8 kpc.

As discussed earlier the resolution of our data prevent us from reliably probing the form of the star formation law on scales less than 300 pc in M51a. As an exploratory exercise we carried out a set of measurements using aperture diameters of $7.''3$ (300 pc), the smallest aperture for which we felt we could reliably measure fluxes, given the beam sizes of our 24 μm, HI, and CO measurements. As before we centered the apertures on the emission peaks in order to obtain reliable photometry. The resulting SFR and gas densities tend to shift to higher values (because the surface densities are more centrally concentrated), but the distribution of points closely follows that of the $13''$ data, with a somewhat larger dispersion about the mean relation. This suggests that any transition in the form of the star formation law from a nonlinear power law relation must occur on scales considerably smaller than 300 pc. However we are reluctant to attach much physical significance to this result, because the apertures are at the limit of the resolution of our infrared, CO, and HI data, and sensitivity limits at this resolution forced us to measure only the brighter star formation peaks, mainly in the spiral arms. The consistency of results is interesting and needs to be followed up on more nearby galaxies where higher spatial resolution can be achieved.

We have also used the FCRAO single-dish CO data of Lord & Young (1990) to examine the star formation law with aperture diameters of 45″ (1850 pc). They obtained measurements at 60 positions, and these cover virtually all of the disk out to the edge of the main spiral pattern (∼5′ diameter). We used the CO measurements from their paper, and also measured CO fluxes from the BIMA SONG maps using their aperture positions and sizes, for 58 objects in common between the two map sets. The two CO datasets give consistent results, but we give preference to the FCRAO data because they have higher signal/noise on these extended scales. We applied the same apertures to our data to measure corresponding HI, Hα, and 24 μm fluxes.

The result of this comparison is shown in Figure 7, which again shows the relationship between SFR surface density and (total) hydrogen surface density, but measured in this case with 1850 pc diameter apertures that fully sample the disk of M51a. Again a strong correlation is observed, with a best-fitting relation: $\log \Sigma_{SFR} = (1.37 \pm 0.03) \log \Sigma_H - (3.90 \pm 0.07)$. The slope of this relation matches within the uncertainties the value of $N = 1.4 \pm 0.15$ seen in global measurements of galaxies (Kennicutt 1998b, §5.3). However the slope of the relation is somewhat shallower than that measured in the 520 pc aperture data (where $N = 1.56 \pm 0.04$), and the zeropoint of the relation is significantly higher, by approximately 0.4 dex (see eq. [7] and Fig. 4). As discussed below (§5.3) these differences in relations can be attributed to different beam filling factors in the respective sets of measurements. Despite these differences it is clear that a Schmidt power law provides a good parametrization of the SFR on scales extending from $300 - 1850$ pc, out to integrated measurements of disks.

The scatter in the 1850 pc relation is roughly a factor of two lower than the corresponding Schmidt law on 520 pc scales. Presumably this results from the averaging over large numbers of individual regions in the larger-aperture measurements. The scatter about the best-fitting relation in Figure 7 (±0.24 dex rms) is larger than the estimated random error in the gas and SFR densities, but it is not significantly larger when systematic errors in the measurements are taken into account, especially when including the extinction corrections.

5.3. Comparison with the Global Schmidt Law for Galaxies

This study was motivated by the discovery of a surprisingly strong and tight Schmidt law relating the disk-averaged SFR surface densities and gas surface densities of galaxies, extending from normal spirals to luminous infrared starburst galaxies (Kennicutt 1998b). So an obvious question is how the local law we have measured in M51a compares to this global relation between entire galaxies. The comparison is shown in Figure 8. Plotted are the SFR and gas surface densities for the 520 pc and 1850 pc data (open circles and solid triangles, respectively). The best fitting solution for the 520 pc data is shown as the solid line, while the dashed line shows the corresponding fit to the 1850 pc data. The dotted line shows the best fit to the integrated Schmidt law for normal galaxies and infrared-selected starburst galaxies from Kennicutt (1998b). Finally the solid blue square in Figure 8 shows the mean integrated SFR and gas surface densities for M51a from the Kennicutt (1998b) analysis.

As expected the local relations in M51a are qualitatively consistent with the global law, but there is a significant offset, with the M51a relations lying lower by 0.46 and 0.39 dex, for the 13″ and 45″ measurements, respectively. We need to bear in mind that the SFR and gas surface densities measured for individual subregions cannot be defined in a way that is entirely consistent with disk-averaged measurements of galaxies; the sample is biased to actively star-forming regions and gas density peaks, the SFR calibrations are different, and the surface area used to convert from SFRs to SFR surface density is somewhat arbitrarily selected. So we would be startled if the relations corresponded exactly, but despite that we find the offset of ∼0.4 dex to be surprising. In the Kennicutt (1998b) study M51a lies 0.24 dex below the overall galaxy sample fit, which may account for part of the difference.

Most of the remaining difference can be attributed to the filling factor of star-forming regions in the disk of M51a. As an illustration, consider an idealized case of a disk containing n identical star-forming regions, each with size r, star formation rate ψ, and gas mass M_g. The disk itself has a radius R_d. The SFR densities and gas densities of the star-forming regions themselves are simply $\psi/\pi r^2$ and $M_g/\pi r^2$, whereas the corresponding SFR and gas surface densities averaged over the entire disk are $n\psi/\pi R_d^2$ and $nM_g/\pi R_d^2$, respectively. Both densities are offset to lower values by the same factor nr^2/R_d^2. However because the slope of the Schmidt law is steeper than a linear relation, the effect of the larger beam sampling will be to offset the disk-averaged densities away from the spatially-resolved Schmidt law. For the case of a Schmidt law with slope $N \sim 1.5$, the approximate offset will be the square root of the individual surface density offsets, or a factor $n^{0.5}r/R_d$. In the case of M51a, $n = 257$, $r = 6\farcs5$, and $R_d = 300''$, and thus we predict that the global relation should be offset from the spatially-resolved relation by ∼0.46 dex. This idealized calculation actually overestimates the offset because in reality there is a considerable amount of star formation and gas at low surface brightness located outside of the 257 regions we measured. When all factors are taken into consideration the observed offset is approximately in agreement with what we would expect from the aperture bias. This same effect can account for the slight offset in zeropoint between the Schmidt law fits to the 520 pc and 1850 pc apertures (§5.2), because the latter measurements cover the inner disk of M51a, so on average the beam filling factor derived for the entire disk applies.

There also is a significant difference in slopes between the 3 relations that are plotted in

Figure 8, ranging from $N = 1.56 \pm 0.04$ for the 520 pc M51a measurements to $N = 1.37 \pm 0.03$ for the 1850 pc M51a data and $N = 1.40 \pm 0.15$ for the global galaxy law. The uncertainties quoted for the M51a measurements only include random errors, while the uncertainty given for the global law is dominated by systematic errors, mainly possible systematic variation in the CO/H_2 X-factor over the large range in gas densities and radiation field environments over which the global law applies. For example a change in X by a factor of two between the IR-luminous starburst galaxies and normal galaxies would be sufficient to increase the slope of the best-fitting global law from $N = 1.4$ to 1.5 (see Kennicutt 1998b). As discussed earlier similar effects may introduce systematic shifts into the relations derived for M51a. In addition, the aperture sampling effects discussed above can also introduce a second-order change in the slope of the Schmidt law if the filling factor of HII regions changes systematically as a function of SFR and gas surface density. For example the fraction of the 45″ beams containing star-forming regions varies from about 10–100% in M51a, with most of the sparsely populated positions occurring at the lowest gas and SFR surface densities. This can shift the slope of the 1850 pc aperture relation by up to −0.2 dex, consistent with the slope offset we observe. As a result, when one takes into account these possible systematic errors the actual uncertainties in the Schmidt law slopes derived for M51a are at least ± 0.1 in N, and hence we are reluctant to attach any astrophysical significance to the differences between the relations seen in Figure 8, until we have an opportunity to study the local relations in more galaxies and construct an improved global relation.

5.4. Alternate Forms of the Star Formation Law

As discussed in §1 the global SFR and gas surface densities of galaxies can be fitted to relations other than a Schmidt law, including the scaling with gas density divided by mean dynamical time (eq. [2]). How well do the resolved observations of M51 fit such a relation? We show the comparison in Figure 9, which plots the SFR densities as a function of the ratio of hydrogen density (HI + H_2) to orbit time for that cloud ($2\pi R/V_{rot}$). We have used different colors to denote the 4 ranges in galactocentric radii, as in Figure 6. The SFR densities and gas densities were calculated as described earlier, and the orbit times were computed using the M51 rotation curve from Sofue et al. (1999). For this model to be valid the slope of the relation is constrained to be unity, so the solid line shows the unit slope line that bisects the data points. Also shown as the dashed line is the global dynamical time relation from Kennicutt (1998b).

Figure 9 reveals a general, qualitative trend for the regions with highest ratio of density to orbit time to have higher SFRs. There is a strong radial segregation of points in this plot, due to the roughly $1/R$ falloff in orbit time over most of the disk. However the slope of the mean relation is far from unity ($\sim$0.65), and the scatter about the mean relation is very large ($\pm$0.4 dex), though not significantly higher than the scatter in the Schmidt law discussed earlier. This relation is also offset below the comparable global relation in Kennicutt (1998b) in this case by a factor of 5 (0.7 dex). We tentatively conclude that although this kinematic star formation law may have some usefulness for characterizing the integrated star formation in galaxies and starbursts, it may be less useful as a description of local star formation in galaxies. We intend to explore this much more carefully when results from the full SINGS dataset are analyzed.

5.5. Evidence for Star Formation Thresholds?

Previous spatially-resolved observations of star formation in galaxies have provided a large body of evidence suggesting that the monotonic behavior of the star formation law at high gas surface densities shows a break at low surface densities, usually characterized as a star formation threshold (e.g., Kennicutt 1989, 1997; Martin & Kennicutt 2001, and references therein). These thresholds have been ascribed to a variety of physical mechanisms, including large-scale gravitational instabilities (e.g., Quirk & Tinsley 1973; Zasov & Simakov 1988; Kennicutt 1989; Hunter et al. 1998; Elmegreen 2002), or molecular or cold gas phase formation thresholds (e.g., Elmegreen & Parravano 1994; Schaye 2004; Blitz & Rosolowsky 2004). Our spatially resolved data allow us to check for the observational signatures of thresholds. In particular we can compare the local gas surface densities with the predicted threshold densities for gravitational instability, and test whether the observations are consistent with that picture.

Examination of Figures 4–7 shows little evidence for any star formation thresholds. The only possible hint might be a handful of regions with the lowest observed SFR surface densities ($\log \Sigma_{SFR} < -2.6$); most of these points lie well below the extrapolated Schmidt law fit, as would be expected if they lay below a threshold. However we believe that most of that trend is due to the sensitivity limit of the CO maps. If there are regions of the disk with lower SFR and gas surface densities they would not be detected in our data.

To test further for threshold effects we calculated for each region the expected critical density using the relation of Kennicutt (1989), which is based on applying the Toomre (1964) gas stability criterion for an isothermal disk of gas clouds:

$$\Sigma_c = \alpha \frac{\kappa c}{\pi G} \tag{9}$$

where Σ_c is the critical (total) gas surface density for star formation, κ is the epicyclic frequency, c is the velocity dispersion of the gas (taken as 6 km s^{-1} following Kennicutt 1989), and α is a scaling constant fitted to the observations (taken as 0.7 following the same paper), in order to reproduce the observed Hα edges of nearby galaxies. The values of κ were calculated from the rotation curve of Sofue et al. (1999). Figure 10 shows the distribution of these threshold normalized surface densities, which correspond roughly to $1/Q$ in terms of the Toomre stability index Q. It is interesting that the distribution shows a strong turnover below a value of unity ($Q > 1$), where one would expect if our sample is limited to regions with active star formation. This result is hardly robust enough to provide firm evidence for thresholds, but its general consistency with the Q-threshold picture is interesting. Of the 257 regions, 29 show local gas surface densities that are below the expected threshold, yet they are forming stars. It is possible that we are seeing a breakdown of the simple threshold model in these cases, but unfortunately they each deviate by less than 1σ of Σ_c; given the large number of points near Σ_c we may well be observing nothing more than the spillover of observational errors in the tails of the distribution. In short our data do not extend deep enough to offer a concise test of the gravitational threshold model, and all that we can say is that the observations are roughly consistent with expectations from that model.

The distribution of HI surface densities elsewhere in M51a (where star formation is not observed) lies almost entirely below the $\Sigma_{gas}/\Sigma_c = 1$ limit, again consistent with the gravitational thresold picture. However we are reluctant to attach much significance to this result, because over much of the disk the CO sensitivity limit lies close to the expected threshold density, so it is difficult to disentangle this incompleteness from a threshold effect. We expect to be able to make more critical tests for threshold effects in some of the other galaxies in the SINGS/SONG sample. In particular, a comparison of the star formation law for the spiral arm and interarm regions is being carried out by de Mello et al. 2007 (in preparation).

6. Discussion and Summary

Our main result is that on spatial scales extending down to at least 500 pc, the SFR surface density is correlated, at least in a statistical sense, with the local gas surface density, following a Schmidt power law:

$$\log \Sigma_{SFR} = (1.56 \pm 0.04)\ \log \Sigma_H - (4.32 \pm 0.09) \tag{10}$$

where Σ_{SFR} is measured in units of M$_\odot$ yr^{-1} kpc^{-2} and Σ_H is measured in units of M$_\odot$ pc^{-2}, and these quantities are sampled with circular apertures of 520 pc diameter. This equation was fitted to the total (atomic plus molecular) hydrogen surface densities, but in M51a the correlation with molecular surface density alone is very similar, with $\log \Sigma_{SFR} = (1.37 \pm 0.03)\ \log \Sigma_{H_2} - (3.78 \pm 0.09)$, as detailed in §5.1. The uncertainties quoted only include formal fitting errors, and do not incorporate any possible systematic errors. If we consider the 1850 pc aperture measurements as a largely independent measurement of the Schmidt law in M51a, then we can use the difference in fits of the 520 pc and 1850 pc data as providing a more realistic indication of the uncertainties.

As we stated at the outset of the paper, this study was mainly intended to build the methodological foundation for a larger study of the SINGS sample in future papers. A key element was the calibration of a combined infrared plus Hα star formation index, which provides more precise Hα extinction corrections for HII regions than have generally been available previously. This in turn makes it possible to quantify the form of the SFR vs gas surface density law on a point-by-point basis in galaxies. We are also extending this basic approach of multi-wavelength SFR tracers to more luminous starbursts (Calzetti et al. 2007) and to galaxies as a whole (Kennicutt et al. 2007, in preparation).

This analyis has revealed other interesting results. We find that the same type of power law relation that describes the global SFRs of galaxies appears to reproduce the star formation law down to local scales of 300 − 1850 pc, approaching at the low extremes the scales of individual giant molecular cloud complexes. Although these relations are defined in terms of total (atomic plus molecular) gas surface densities, in M51a they mainly trace an underlying correlation with the molecular surface density component. This must result at least partly from the dominance of molecular gas in M51a. By contrast the local SFR surface density is virtually uncorrelated with the surface density of HI on these scales.

As mentioned earlier, when the global, disk-averaged SFR surface densities of galaxies are correlated with the disk-averaged atomic, molecular, and surface densities, the strongest correlations are with the total gas density (Buat et al. 1989, Kennicutt 1989, 1998b). Indeed among normal star-forming disk galaxies the SFR surface density is only weakly correlated at best with the CO-inferred molecular surface density (Kennicutt 1989), quite the opposite of what is observed here on a point-by-point basis in M51a. On the other hand, in infrared-luminous starburst galaxies, which typically contain dense compact gas disks, the SFR and molecular surface densities are tightly correlated. So it may well be that the behaviors of the spatially-resolved and disk-integrated SFR vs molecular surface density relations are consistent when similar regimes in surface density are compared. This raises a separate question of whether the tightness of the Σ_{SFR} *vs* Σ_{H_2} at high surface density arises because of a fundamental correlation between the SFR and the molecular gas phase, or alternatively from an underlying correlation of the SFR with the total gas density, which manifests itself as a correlation with Σ_{H_2} only when the gas is predominantly molecular? We hope to address this question by extending our analysis to galaxies with a larger atomic gas component.

Although we have observed broad consistency in the form of the Schmidt law across a wide range of physical scales, as discussed in §5.3 we do observe significant shifts in the zeropoint (and possibly the slope) with scale size. Our results suggest that the correlation between SFR and gas surface densities on small scales defines an intrinsic Schmidt law, and when these surface densities are measured with larger measuring apertures (which include an increasing fraction of area devoid of star-forming regions and gas), the zeropoint of the Schmidt law becomes larger, because of the nonlinear slope of the relation. So which relation is more fundamental? It is tempting to define the spatially-resolved relation as the physically fundamental one, but this relation is based on a highly biased subsampling of the disk, limited to the most massive GMC complexes and giant HII regions. The larger aperture measurements provide a completely unbiased sampling of the disk, but are based on averages of SFR and gas surface densities which vary locally by orders of magnitude within the measuring apertures. The most important lesson is that this scale dependence of the Schmidt law must be taken into account when it is applied to a dataset or to a theoretical model. For example, our results show that the SFR surface density predicted for a region of fixed gas surface density can differ by more than a factor of two, depending on whether the size of the region of interest is $\sim$0.5 kpc or averaged over the entire disk of a galaxy.

Eventually we hope that data of this kind will shed new insights into the physical origins of the observed star formation law. A rigorous *ab initio* theory for star formation on these scales is not yet in place, so it is not entirely clear what theory would predict for the form of the local star formation law. Nevertheless our observations provide some tantalizing clues. Since our measurements have been made with fixed-diameter apertures, the gas surface densities can be readily converted to total gas masses, and the combination of Hα and infrared luminosities provides a direct measurement of the ionizing flux of the embedded stars. The nonlinearity in the observed Schmidt law thus implies that the present instantaneous SFR per unit gas mass increases in the more massive clouds (or complexes). It is very tempting to attribute this result to a possible increase in the star formation efficiency in more massive clouds, that is, a higher fraction of stars formed in the more massive clouds. However this direct extrapolation is not valid, because the measured ionizing fluxes only provide information at most on the mass of recently formed O-stars in the clouds, and not on the total mass of stars (of all stellar masses) formed over the lifetimes of the clouds. One could explain a $N \sim 1.5$ Schmidt law even if the star formation efficiency were the same for all cloud masses and gas surface densities, if for example the star-forming lifetimes of massive clouds were systematically lower than for low-mass clouds, or if the period of peak formation of O-stars decreased with increasing cloud mass. Without further observational constraints on these time scales one cannot draw any direct association between the slope of the star formation law and the constancy (or not) of the cloud-averaged star formation efficiency. However the extension of the nonlinear Schmidt law down to linear scales of 500 pc and cloud mass scales of order $10^6 - 10^7$ $M_\odot$ strongly hints at either an increasing star formation efficiency or a shorter star formation time scale with increasing cloud mass. An important next step would be an extension of this analysis to nearer galaxies with lower limiting cloud masses and SFRs, and to Galactic clouds, where direct information on stellar ages is available.

This case study of M51a has illustrated the value of spatially-resolved infrared, Hα, HI, and CO observations of nearby galaxies for constraining the form and physical nature of the star formation law. However, much future work is needed on this problem. Within the larger SINGS project we plan to extend this analysis to approximately 15 other galaxies for which high quality CO, HI, Hα, and Spitzer 24 μm data are available. These galaxies cover a wide range of types and gas disk properties, and the extended physical coverage may resolve some of the questions and selection effects that have muddied the interpretation of these data. Looking further ahead, the study of the star formation law in galaxies remains limited in large part by the spatial resolution and sensitivity of the molecular gas data, even with the superb BIMA data in hand. Follow-up deeper mapping of a handful of galaxies, extending to limiting column densities below those expected for gravitational stability would allow for a much more physically meaningful interpretation of the observed SFR law. Finally, independent measures of extinction in some of these galaxies (redundant with the infrared + Hα extinctions derived here) would provide much better constraints on the random and systematic measurements in our SFR measurements and the dispersion of the star formation law. The results of such efforts will have far-reaching applicability to the understanding of star formation in galaxies and the formation and evolution of galaxies.

We would like to acknowledge valuable discussions with a number of colleagues, including Ayesha Begum, Hsiao-Wen Chen, Cathie Clarke, Crystal Martin, Phil Solomon, and Art Wolfe. We thank the anonymous referee for a careful reading of the manuscript. This work is based in part on observations made with the Spitzer Space Telescope, which is operated by the Jet Propulsion Laboratory, California Institute of Technology under a contract with NASA. Support for this work was provided by NASA through an award issued by JPL/Caltech.

REFERENCES

Aalto, S., Hüttemeister, S., Scoville, N. Z., & Thaddeus, P. 1999, ApJ, 522, 165

Allen, R.J., Knapen, J.H., Bohlin, R., & Stecher, T.P. 1997, ApJ, 487, 171

Alonso-Herrero, A., Rieke, G.H., Rieke, G.J., Colina, L., Pérez-González, P.G., & Ryder, S.D. 2006, ApJ, 650, 835

Baars, J. W. M., Genzel, R., Pauliny-Toth, I. I. K., & Witzel, A. 1977, A&A, 61, 99

Bell, E.F. 2003, ApJ, 586, 794

Bendo, G.J. et al. 2006, ApJ, 652, 283

Blitz, L., Fukui, Y., Kawamura, A., Leroy, A., Mizuno, N., & Rosolowsky, E. 2007, in Protostars and Planets V, B. Reipurth, D. Jewitt, and K. Keil (eds.), University of Arizona Press, Tucson, 81

Blitz, L., & Rosolowsky, E. 2004, ApJ, 612, L29

Bloemen, J.B.G.M. et al. 1986, A&A, 154, 25

Boissier, S., Prantzos, N., Boselli, A., & Gavazzi, G. 2003, MNRAS, 346, 1215

Bresolin, F., Kennicutt, R.C., & Garnett, D.R. 1999, ApJ, 510, 104

Bresolin, F., Garnett, D.R., & Kennicutt, R.C. 2004, ApJ, 615, 228

Buat, V., Deharveng, J.M., & Donas, J. 1989, A&A, 223, 42

Calzetti, D. et al. 2005, ApJ, 633, 871 (Paper I)

Calzetti, D. et al. 2007, ApJ, in press (astro-ph/0705.3377)

Cardelli, J. A., Clayton, G. C., & Mathis, J. S. 1989, ApJ, 345, 245

Cerviño, M., Valls-Gabaud, D., Luridiana, V., & Mas-Hesse, J.M. 2002, A&A, 381, 51

Dale, D.A. et al. 2007, ApJ, 655, 863

Draine, B.T. et al. 2007, ApJ, 663, 866

Elmegreen, B.G. 2002, ApJ, 577, 206

Elmegreen, B.G., & Parravano, A. 1994, ApJ, 435, L121

Engelbracht, C.W. et al. 2007, PASP, in press (astro-ph/0704.2195)

Garcia-Burillo, S., Guelin, M., & Cernicharo, J. 1993, A&A, 274, 123

Garnett, D.R., Kennicutt, R.C., & Bresolin, F. 2004, ApJ, 607, L21

Gordon, K.D., Clayton, G.C., Witt, A.N., & Misselt, K.A. 2000, ApJ, 533, 236

Gordon, K.D. et al. 2004, ApJS, 154, 215

Gordon, K.D. et al. 2005, PASP, 117, 503

Helfer, T. T., et al. 2001, Ap&SS, 276, 1131

Helfer, T. T., Thornley, M. D., Regan, M. W., Wong, T., Sheth, K., Vogel, S. N., Blitz, L., & Bock, D. C.-J. 2003, ApJS, 145, 259

Heyer, M.H., Corbelli, E., Schneider, S.E., & Young, J.S. 2004, ApJ, 602, 723

Hirashita, H., Buat, V., & Inoue, A.K. 2003, A&A, 410, 83

Hunter, D.A., Elmegreen, B.G., & Baker, A.L. 1998, ApJ, 493, 595

Hunter, S.D. et al. 1997, ApJ, 481, 205

Iglesias-Páramo, J. et al. 2006, ApJS, 164, 38

Jorsater, S., & van Moorsel, G. A. 1995, AJ, 110, 2037

Kay, S.T., Pearce, F.R., Frenk, C.S., & Jenkins, A. 2002, MNRAS, 330, 113

Kennicutt, R.C. 1984, ApJ, 287, 116

Kennicutt, R.C. 1988, ApJ, 334, 144

Kennicutt, R.C. 1989, ApJ, 344, 685

Kennicutt, R.C. 1997, in The Interstellar Medium in Galaxies, ed. J.M. van der Hulst, Dordrect: Kluwer, Ap & Sp Sci Lib, Vol 219, p171

Kennicutt, R.C. 1998a, ARA&A, 36, 189

Kennicutt, R.C. 1998b, ApJ, 498, 541

Kennicutt, R.C. et al. 2003, PASP, 115, 928

Komugi, S., Sofue, Y., Nakanishi, H., Onodera, S., & Egusa, F. 2005, PASJ, 57, 733

Kuno, N., Nakai, N., Handa, T., & Sofue, Y. 1995, PASJ, 47, 745

Lord, S.D., & Young, J.S. 1990, ApJ, 356, 135

Martin, C.L., & Kennicutt, R.C. 2001, ApJ, 555, 301

Nakai, N., & Kuno, N. 1995, PASJ, 47, 761

Osterbrock, D.E., & Ferland, G.J. 2006, Astrophysics of Gaseous Nebulae and Active Galactic Nuclei, Mill Valley: University Science Books

Popescu, C. C., & Tuffs, R. J. 2002, Reviews in Modern Astronomy, 15, 239

Quillen, A.C., & Yukita, M. 2001, AJ, 121, 2095

Quirk, W.J., & Tinsley, B.M. 1973, ApJ, 179, 69

Schaye, J. 2004, ApJ, 609, 667

Schmidt, M. 1959, ApJ, 129, 243

Schmidt, M. 1963, ApJ, 137, 758

Schuster, K. F., Kramer, C., Hitschfeld, M., Garcia-Burillo, S., & Mookerjea, B. 2007, A&A, 461, 143

Scoville, N.Z., Polletta, M., Ewald, S., Stolovy, S. R., Thompson, R., & Rieke, M. 2001, AJ, 122, 3017

Scoville, N.Z., & Young, J.S. 1983, ApJ, 265, 148

Shaya, E.J., & Federman, S.R. 1987, ApJ, 319, 76

Silk, J. 1997, ApJ, 481, 703

Sofue, Y., Tutui, Y., Honma, M., Tomita, A., Takamiya, T., Koda, J., & Takeda, Y. 1999, ApJ, 523, 136

Strong, A.W. et al. 1988, A&A, 207, 1

Tilanus, R.P.J, Allen, R.J., van der Hulst, J.M., Crane, P.C., & Kennicutt, R.C. 1988, ApJ, 330, 667

Tilanus, R.P.J, & Allen, R.J. 1991, A&A, 244, 8

Toomre, A. 1964, ApJ, 139, 1217

Tully, R.B. 1974, ApJS, 27, 437

van der Hulst, J.M., Kennicutt, R.C., Crane, P.C., & Rots, A.H. 1988, A&A, 195, 38

Walter, F., & Brinks, E. 1999, AJ, 118, 273

Walter, F., Brinks, E., de Blok, W.J.G., Thornley, M.D., & Kennicutt, R.C. 2005, in Extraplanar Gas, ed. R. Braun, ASP Conf Ser 331, p269

Wong, T., & Blitz, L. 2002, ApJ, 569, 157

Wu, J., Evans, N.J., Gao, Y., Solomon, P.M., Shirley, Y.L., & Vanden Bout, P.A. 2005, ApJ, 635, L173

Zasov, A., & Simakov, S.G. 1988, Astrophysics, 29, 518

Zhang, Q., Fall, S.M., & Whitmore, B.C. 2001, ApJ, 561, 727

This preprint was prepared with the AAS LaTeX macros v5.2.

Table 1. Aperture Photometry[1]

ID	RA J2000	Dec J2000	D_{ap} $''$	$\log L_{H\alpha}$[2] $\mathrm{ergs\,s^{-1}}$	$\log L_{Pa\alpha}$[2] $\mathrm{ergs\,s^{-1}}$	$\log L_{24}$[3] $\mathrm{ergs\,s^{-1}}$	$\log \Sigma_{SFR}$[4]	$\log N_{HI}$ $\mathrm{H\,cm^{-2}}$	$\log N_{H2}$ $\mathrm{H_2\,cm^{-2}}$	$\log \Sigma_H$ $\mathrm{M_\odot\,pc^{-2}}$
1	13:29:51.5	47:11:43	13	38.86	38.84	41.17	-0.50±0.025	20.26	21.98	2.19±0.094
2	13:29:52.8	47:11:33	13	39.09	38.83	41.16	-0.57±0.026	19.65	22.00	2.21±0.090
3	13:29:52.3	47:11:27	13	38.90	38.78	41.09	-0.57±0.028	20.68	22.17	2.38±0.063
4	13:29:51.8	47:11:23	13	38.74	38.67	40.92	-0.68±0.037	20.65	22.10	2.31±0.073
5	13:29:53.1	47:11:21	13	38.73	38.44	40.99	-0.96±0.061	20.76	22.23	2.44±0.055
6	13:29:53.8	47:11:24	13	38.86	38.59	41.08	-0.80±0.044	20.46	22.28	2.49±0.050
7	13:29:52.7	47:12:03	13	39.04	38.92	41.24	-0.45±0.021	20.71	22.36	2.57±0.042
8	13:29:52.2	47:11:58	13	39.19	39.04	41.36	-0.33±0.016	20.62	22.47	2.68±0.032
9	13:29:52.0	47:12:05	13	39.17	38.95	41.32	-0.43±0.019	20.64	22.31	2.52±0.046
10	13:29:51.4	47:12:02	13	39.11	38.91	41.36	-0.47±0.021	20.77	22.39	2.60±0.039

[1]A complete listing of data in this table, including 13″ and 45″ aperture photometry can be found in the on-line edition.

[2]Ionized gas luminosities have been corrected for Galactic foreground extinction $E(B-V)_{MW} = 0.037$, but otherwise have not been corrected for extinction.

[3]Defined as νL_ν at $24\,\mu$m

[4]In units of $\mathrm{M_\odot\,yr^{-1}\,kpc^{-2}}$. SFRs for objects with Paα photometry were corrected for extinction using the Paα/Hα ratio. Otherwise SFRs were corrected for extinction using the $24\,\mu$m/Hα ratio, as described in the text.

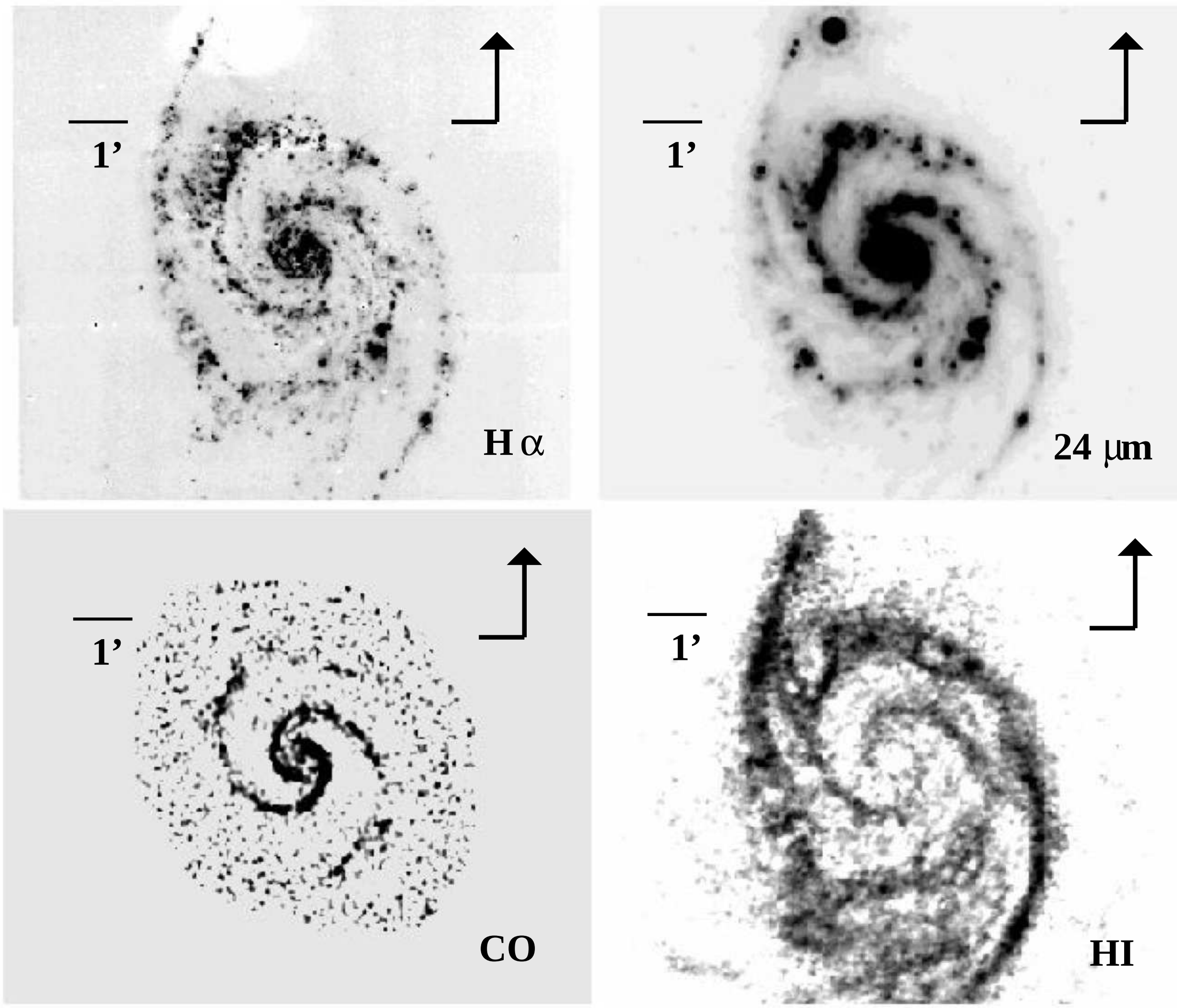

Fig. 1.— M51 as observed in Hα, 24 μm continuum, CO, and HI. North is up (arrow) and east is to the left. The horizontal bars in the left corner of each panel indicate an angular scale of 1 arcminute (2.5 kpc). These are shown to illustrate qualitatively the relative distributions of the cold gas and star formation tracers.

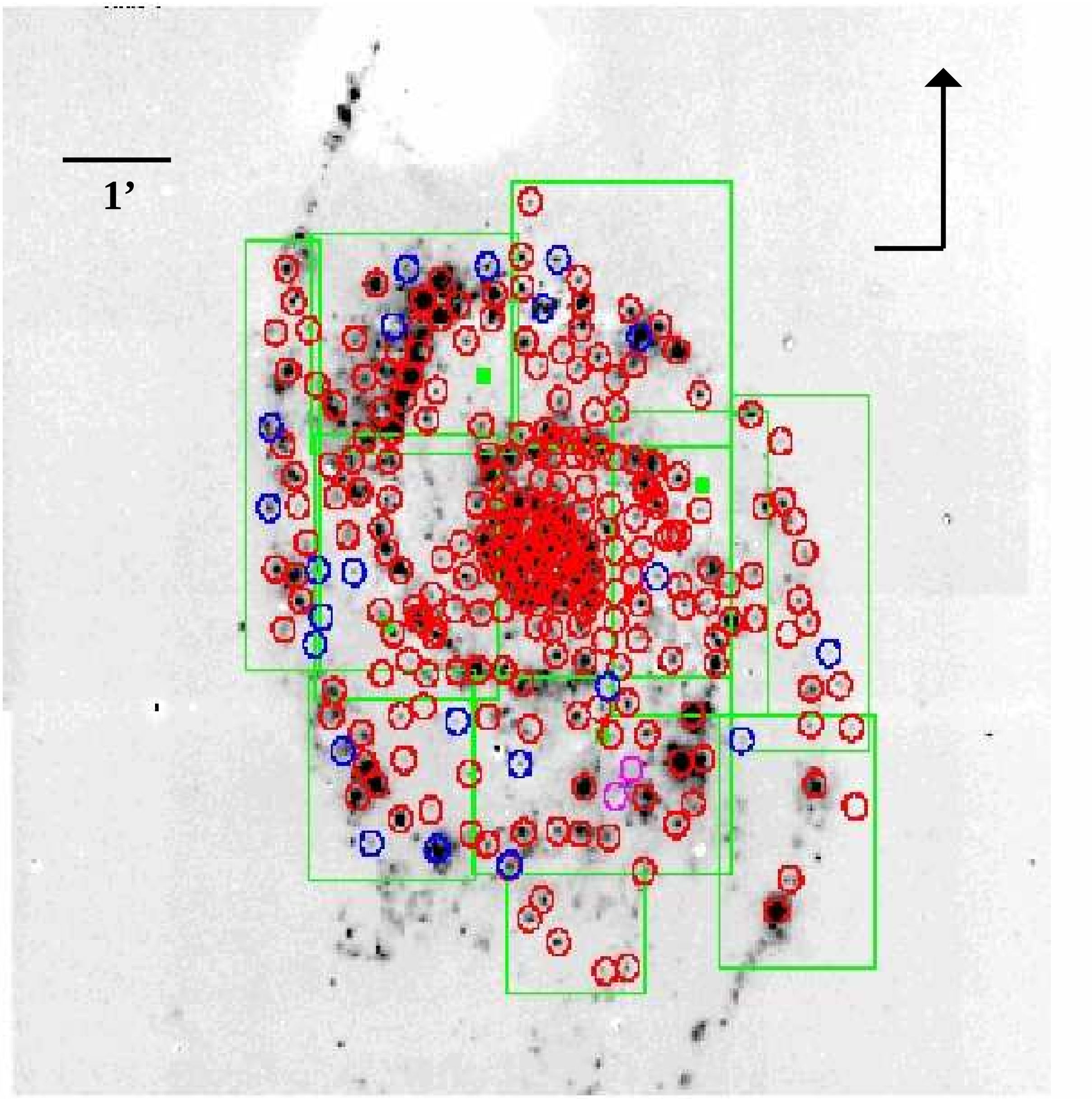

Fig. 2.— Continuum-subtracted Hα image of M51 with the 13$''$ (520 pc) measuring apertures shown. Red circles denote regions detected in CO, HI, Hα, and 24 μm. Blue circles denote regions with CO upper limits (but detected at all other wavelengths), and the two magenta circles denote CO sources without significant detections of Hα or infrared emission. The rectangles show regions selected for background determinations, as described in the text.

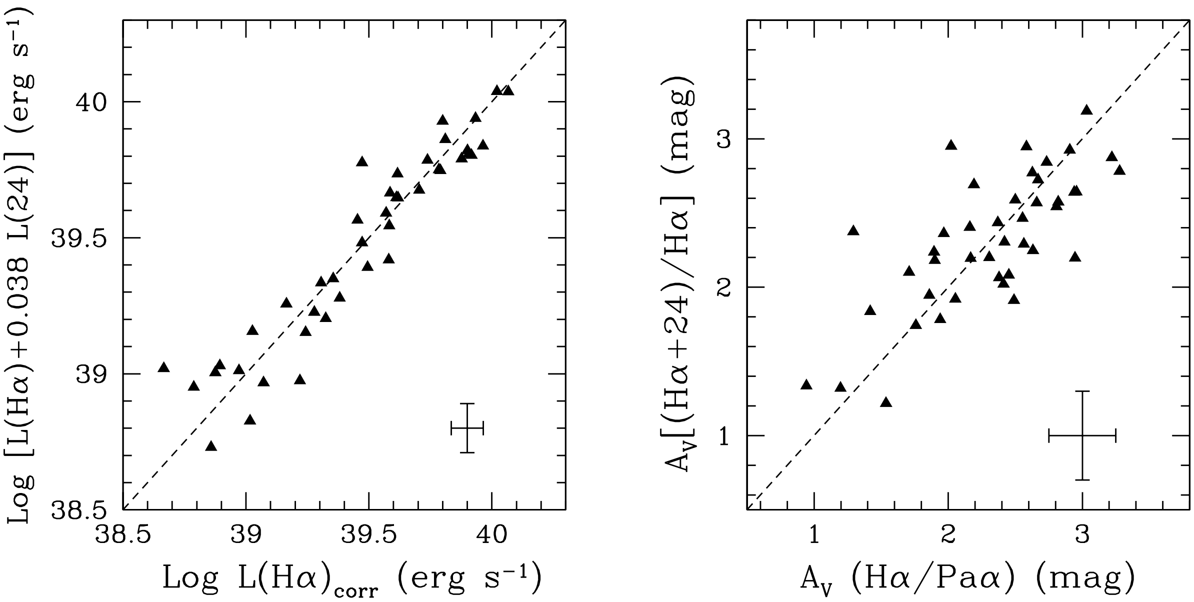

Fig. 3.— Left: Comparison of attenuation-corrected Hα luminosities for 42 HII regions in the inner disk of M51, using a weighted sum of observed Hα and 24 μm luminosities, vs independently extinction-corrected Hα luminosities, derived from the Hα/Paα flux ratios. The line shows the median fit with a slope forced to unity. The error bars show typical uncertainties for the measurements. Right: Comparison of the corresponding visual extinctions for the same objects, as derived from the weighted sum of Hα and 24 μm fluxes, vs those derived from Hα/Paα flux ratios.

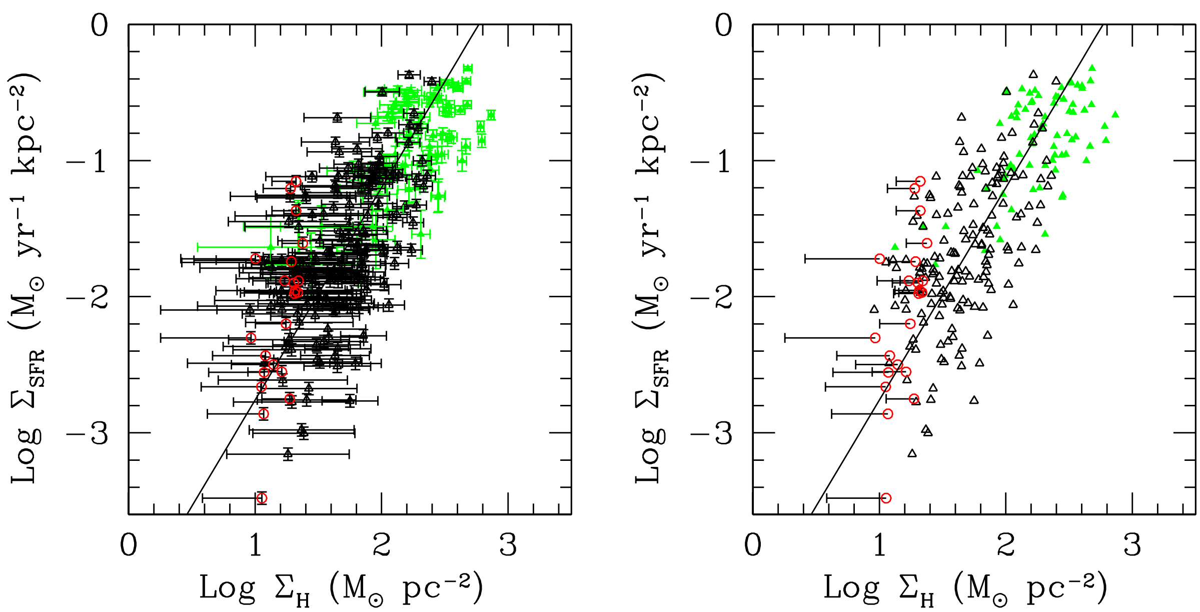

Fig. 4.— Relationship between SFR surface density and total (atomic plus molecular) hydrogen surface density for 257 HII regions and infrared sources measured in the central 350″ region of M51 (the area covered in CO by BIMA SONG). Solid green triangles denote SFRs derived from extinction-corrected Paα fluxes, all in the central 144″, while open black triangles denote SFRs determined from combined 24 μm and Hα fluxes, using the method described in §4. Open (red) circles denote regions with only 3-σ upper limits in CO (see text).

The fluxes were measured with aperture diameters of 13″ (520 pc). The line shows a best fitting power law with slope $N = 1.56$. Points in the two panels are identical except for the inclusion of error bars, for the sake of clarity.

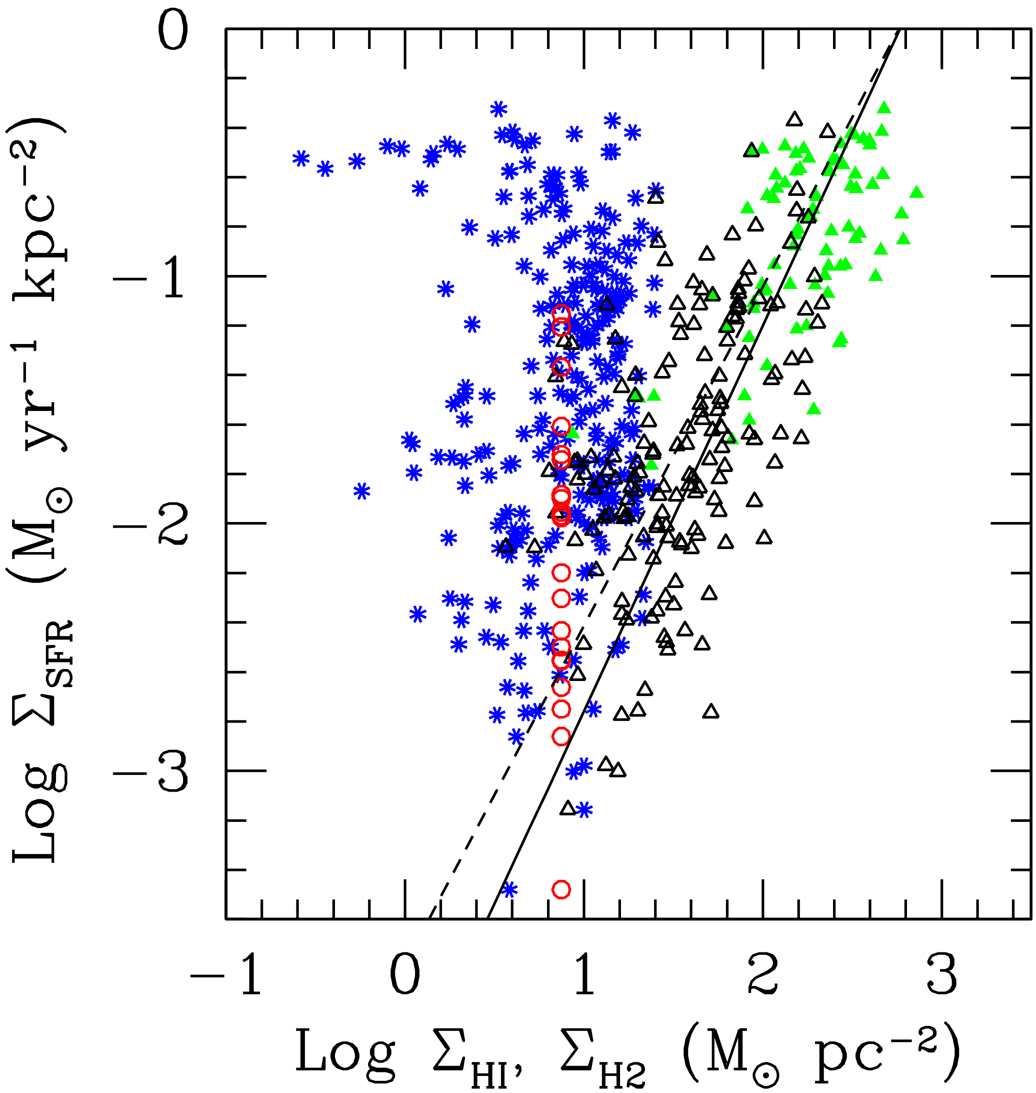

Fig. 5.— Relation between local SFR density and molecular and atomic hydrogen surface densities separately. The solid green and open black triangles denote H_2 surface densities (see Fig. 4), with open red circles indicating CO upper limits (same symbol notation as for Figure 4). Blue asterisks show the corresponding relation between SFR surface densities and HI surface densities. The dashed line shows the best bivariate least squares fit to the molecular densities alone. The fit to total gas density (see Figure 4) is shown for reference as the solid line.

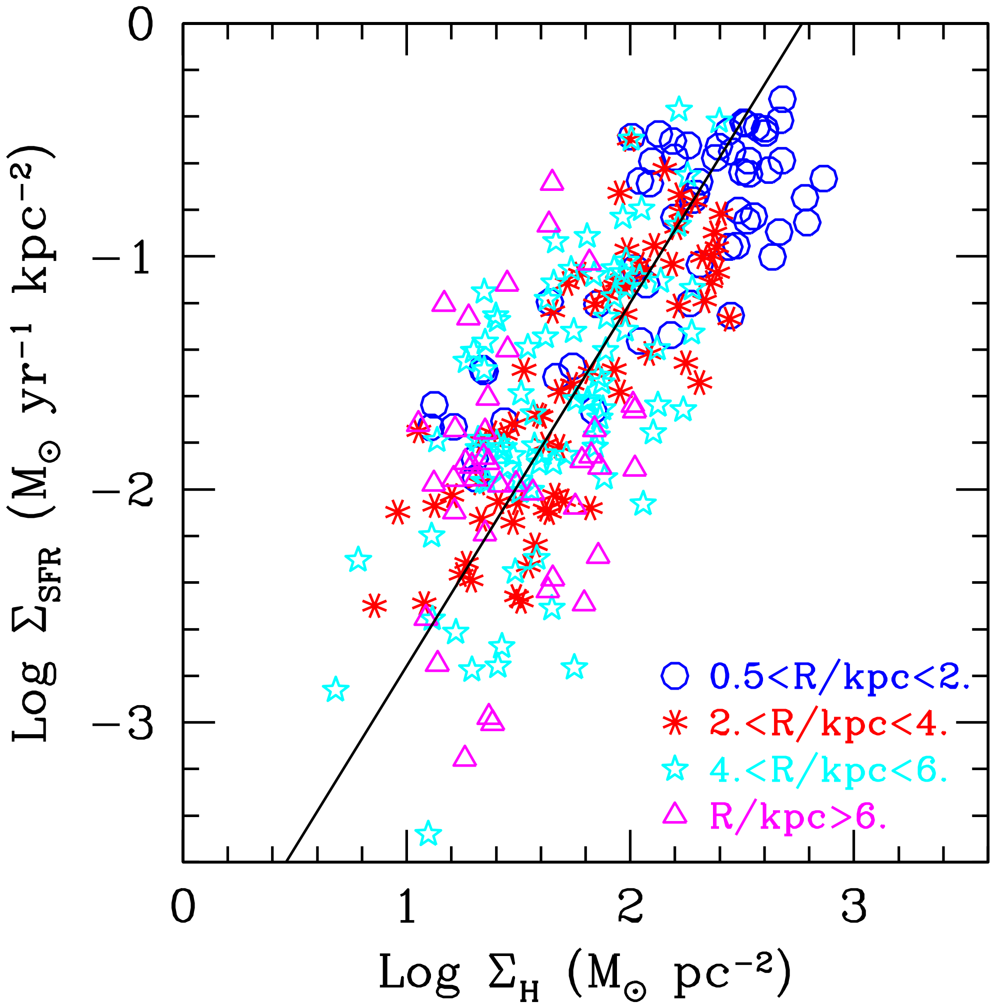

Fig. 6.— Same data as shown in Figure 4, but with points coded by galactocentric radius.

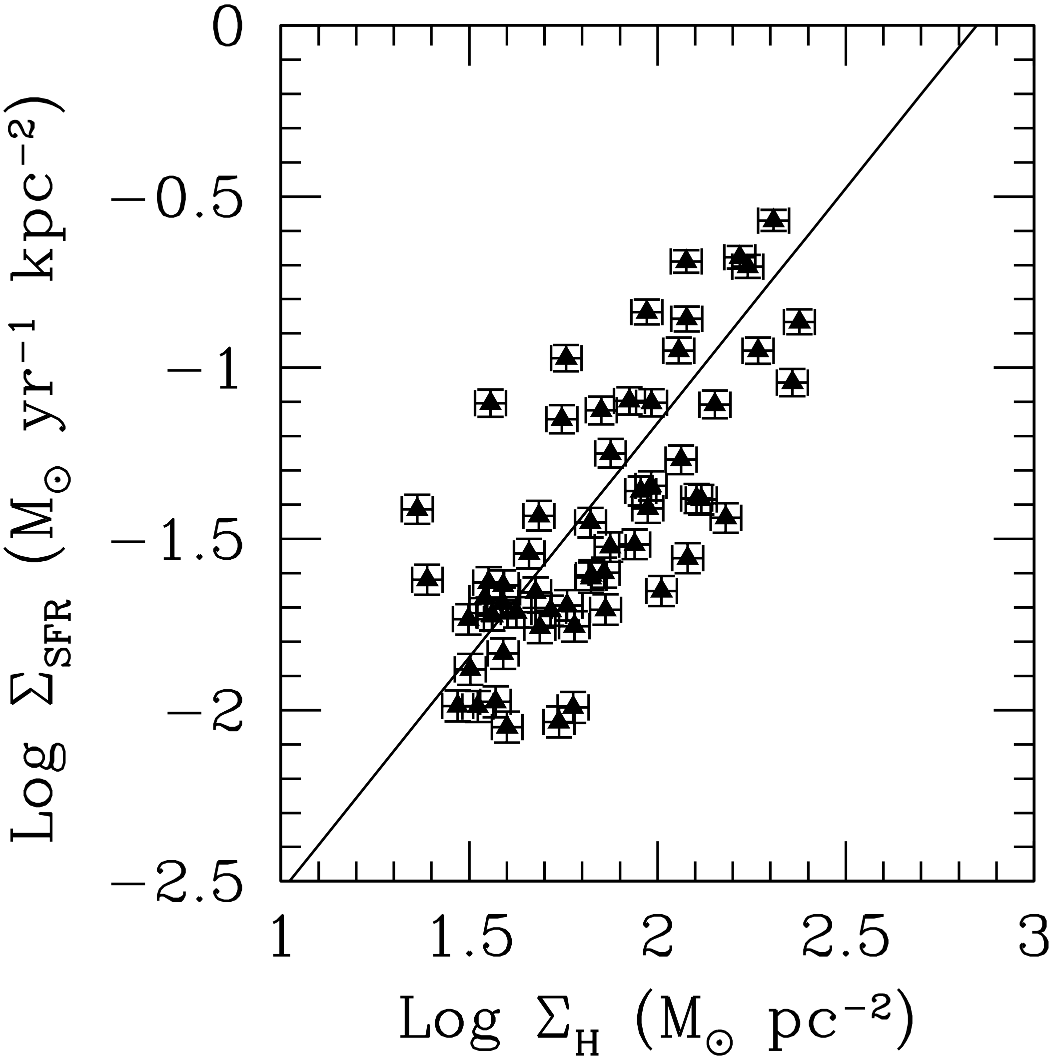

Fig. 7.— Relation between SFR and total gas surface densities using CO and HI data from Lord & Young (1990), with aperture diameters of 45″ (1850 pc). The solid line shows a best bivariate fit with slope $N = 1.37$.

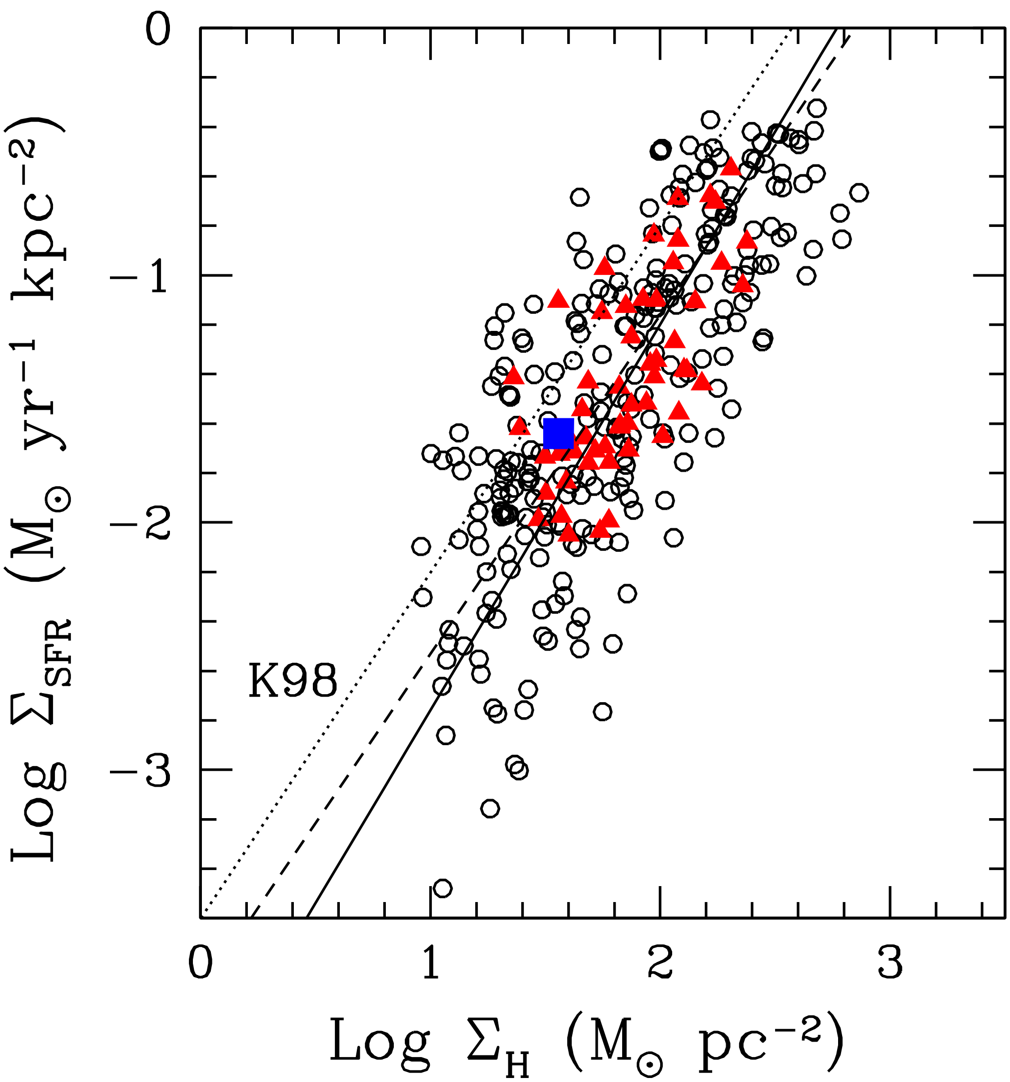

Fig. 8.— Comparison of the Schmidt law measured for M51 using 520 pc (13″) apertures (open black circles) and 1850 pc (45″) apertures (solid red triangles), with the best fitting power-law fits shown with solid and dashed lines, respectively. Shown for comparison by the upper dotted line is the disk-averaged Schmidt law for normal and starburst galaxies from Kennicutt (1998b). The large blue square shows the disk-averaged SFR and gas density for M51 as measured in that paper.

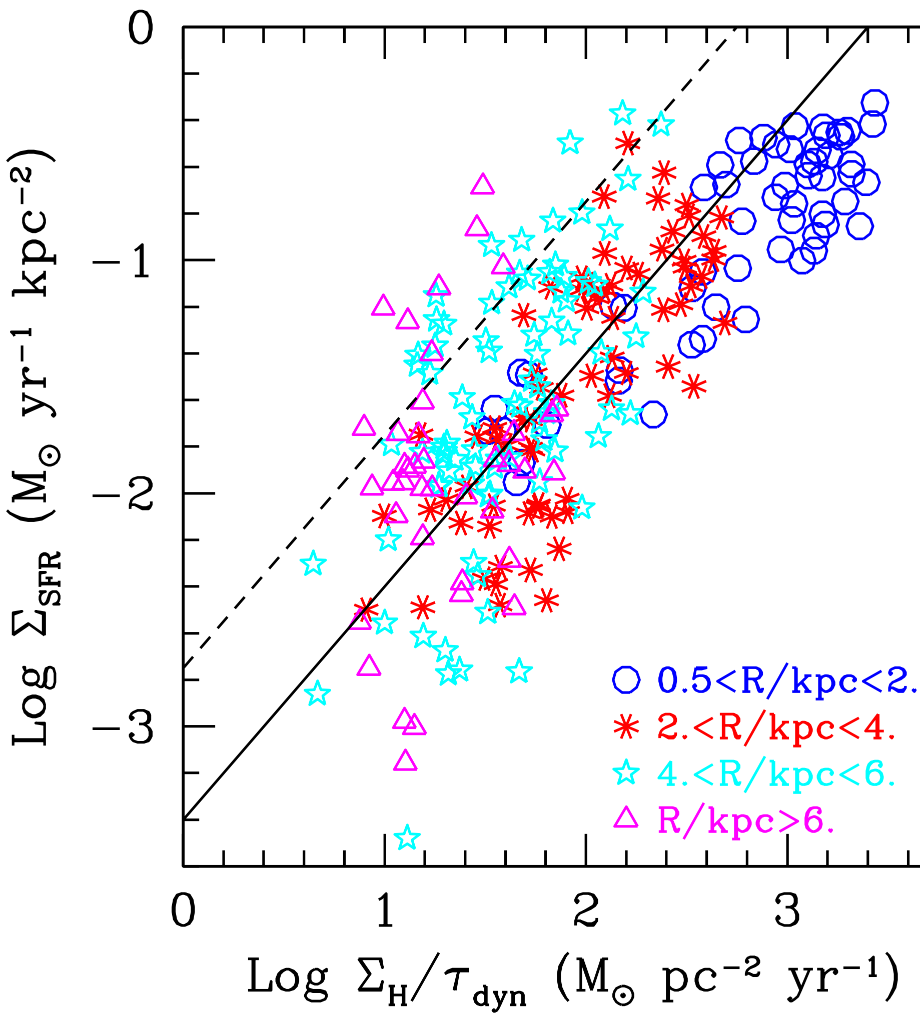

Fig. 9.— SFR surface densities plotted as a function of the ratios of gas surface density to orbit time (equation [2]). The 520 pc aperture data are shown, and are color coded by galactocentric radius in kpc, as in Figure 6. The solid line is the best fit relation with slope constrained to unity. Note the deviation from linear slope at constant radius, though the large-scale distribution of points traces a roughly linear relation. The dashed line shows the comparable fit to the disk-averaged SFRs in Kennicutt (1998b).

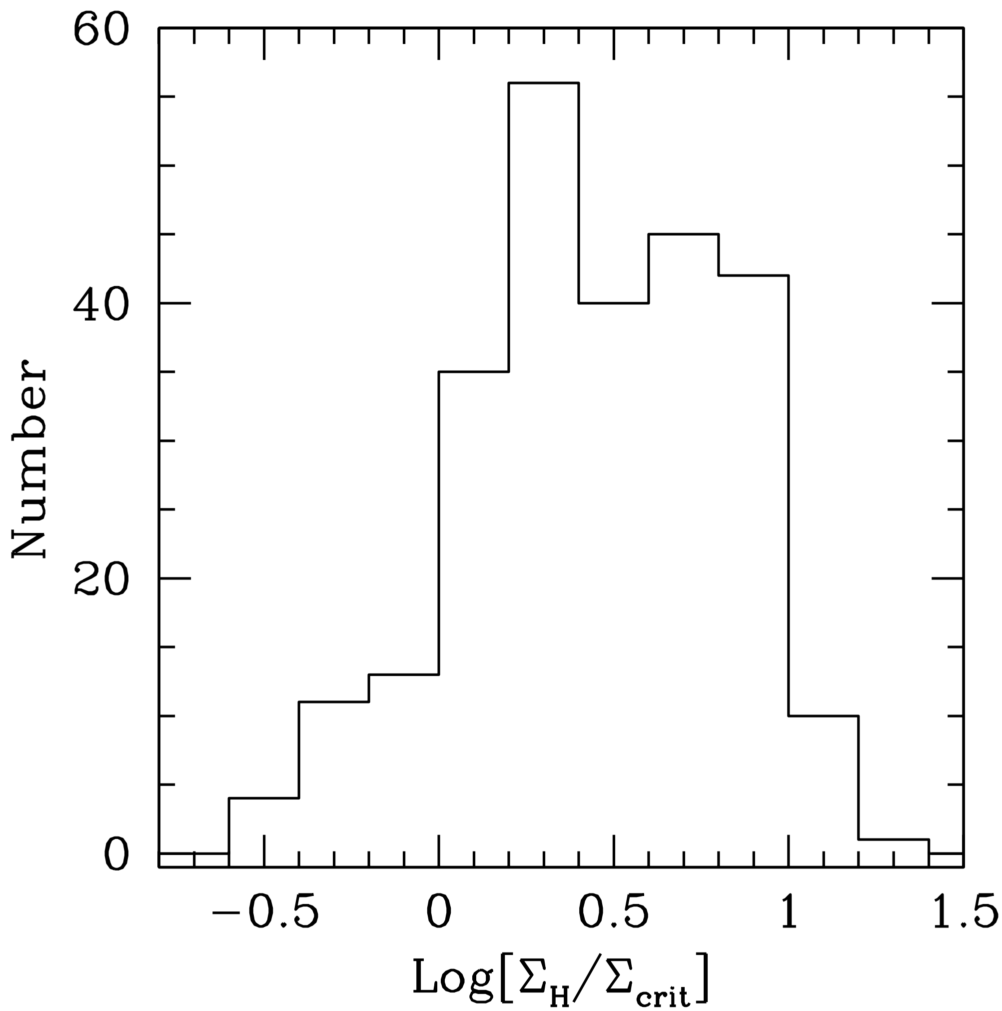

Fig. 10.— Distribution of the total gas surface densities of the 257 regions in M51 studied here (520 pc apertures), normalized in each case to the local critical density for gravitational stability, as defined in eq. (9). Expressed in terms of the Toomre stability parameter Q the ratio plotted corresponds roughly to $1/Q$. The densities include molecular and atomic hydrogen, multiplied by a factor of 1.38 to account for helium and metals. Note the truncation near a value of SFR densities for $Q < 1$.